Analyst

CRITICAL REVIEW

View Article Online
View Journal | View Issue

Cite this: *Analyst*, 2018, **143**, 2723

In vitro and *ex vivo* measurement of the biophysical properties of blood using microfluidic platforms and animal models†

Yang Jun Kang [a] and Sang-Joon Lee *[b]

Received 6th February 2018,
Accepted 11th April 2018

DOI: 10.1039/c8an00231b

rsc.li/analyst

Haemorheologically impaired microcirculation, such as blood clotting or abnormal blood flow, causes interrupted blood flows in vascular networks. The biophysical properties of blood, including blood viscosity, blood viscoelasticity, haematocrit, red blood bell (RBC) aggregation, erythrocyte sedimentation rate and RBC deformability, have been used to monitor haematological diseases. In this review, we summarise several techniques for measuring haemorheological properties, such as blood viscosity, RBC deformability and RBC aggregation, using *in vitro* microfluidic platforms. Several methodologies for the measurement of haemorheological properties with the assistance of an extracorporeal rat bypass loop are also presented. We briefly discuss several emerging technologies for continuous, long-term, multiple measurements of haemorheological properties under *in vitro* or *ex vivo* conditions.

1. Introduction

Negative health behaviours (smoking, physical inactivity, poor diet and inappropriate weight) and factors (cholesterol, blood pressure and glucose) increase the risk of cardiovascular diseases (CVDs).[1] CVDs are the leading cause of death in advanced countries, and they accounted for 31.5% of all deaths worldwide in 2013.[1] CVDs, including stroke, atherosclerosis, coronary heart disease and myocardial infarction, suddenly occur without any noticeable symptoms and consequently lead to serious complications or unexpected deaths. In particular, haemorheologically impaired microcirculation (blood clotting or abnormal blood flow) interrupts blood flows in vascular networks. Biochemical analyses are used to diagnose CVDs by checking several parameters, including biomarkers, cholesterol, glucose or DNA. However, biochemical

[a]*Department of Mechanical Engineering, Chosun University, Gwangju, Republic of Korea*
[b]*Department of Mechanical Engineering, Pohang University of Science and Technology (POSTECH), Pohang, Republic of Korea. E-mail: sjlee@postech.ac.kr; Fax: +82-54-279-3199*

†Electronic supplementary information (ESI) available. See DOI: 10.1039/c8an00231b

Yang Jun Kang

Yang Jun Kang received his Ph.D. degree in 2011 from the School of Mechatronics of Gwangju, Institute of Science and Technology, South Korea. Since 2014, he has been working as assistant professor in Chosun University, South Korea. Before he joined this university, he worked as a research professor in the Center for Biofluid and Biomimic Research in POSTECH, South Korea. His research interests lie in hemorheological and hemodynamic analyses using microfluidic devices.

Sang-Joon Lee

Sang-Joon Lee received his Ph.D. degree in 1986 from the Department of Mechanical Engineering from KAIST, Korea. He joined as a professor in the Mechanical Engineering Department of POSTECH in 1987 and was a director of the Center for Biofluid and Biomimic Research. He is now a University Professor at POSTECH. His research interests lie in biofluid flows, microfluidics, flow visualization, biomimetics, and flow control.

analyses do not provide sufficient diagnostic information on vascular blockage or blood clotting in advance. Thus, early detection of CVD remains difficult. On the basis of close relationships between CVDs and haemorheological properties, several research groups recently demonstrated that the haemorheological characteristics of blood flows are significantly correlated with CVDs.[2] Lowe *et al.*[3] statistically reviewed the significant association between biophysical properties of blood [haematocrit, plasma viscosity, blood viscosity and erythrocyte sedimentation rate (ESR)] and coronary heart disease. Yayan[4] reported that the specificity and sensitivity of ESR for coronary heart disease are 70.59% and 67.65%, respectively. Given that the biophysical properties of blood (haematocrit, blood viscosity, plasma viscosity, blood viscoelasticity, RBC aggregation, RBC deformability and ESR) provide valuable information on haematological disorders or diseases, they have been recommended for use in monitoring or diagnosing patients with CVDs.

In 1952, Copley introduced the word 'haemorheology' and defined it as the study of how blood and blood vessels function and interact as parts of living organs.[5] In other words, haemorheology deals with blood flow and deformation of blood cells, blood compositions and blood vessels. Blood is composed of cell components [red blood cells (RBCs), white blood cells (WBCs), and platelets] and plasma. As shown in Fig. 1, haemorheological properties are represented by several factors, including haematocrit (Hct),[6,7] cell components (RBCs, WBCs and platelets), cell-free layer,[8,9] blood vessel diameter[10,11] and plasma proteins. RBCs are strongly related to the biophysical properties of blood because they constitute approximately 45% of blood volume. Instead of counting the number of RBCs in a specific volume, haematocrit, which is defined as the volume ratio of RBCs to the total volume, has been widely used. Secondly, the RBC membrane is made up of a lipid bilayer and has several tiny gates for the transport of ions, molecules and signals. This membrane behaves like a mechanical structure under an external force or stimuli. An individual RBC is elongated and aligned with the shearing blood flow. RBC membranes exhibit tank-treading or flexible motion.[12] The surface properties of RBC membranes are crucial in blood viscosity determination and RBC aggregation. A high stiffness of RBC membranes leads to increased blood viscosity or decreased RBC aggregation. Thirdly, plasma proteins are composed of albumin, fibrinogen and immunoglobin. Among these plasma proteins, fibrinogen, which participates in clotting formation, contributes to RBC aggregation and blood viscosity significantly. Haemorheological properties depend on the molecular weight and morphological structure of plasma proteins. In addition, inflammations or tissue injuries contribute to changes in plasma proteins.[13]

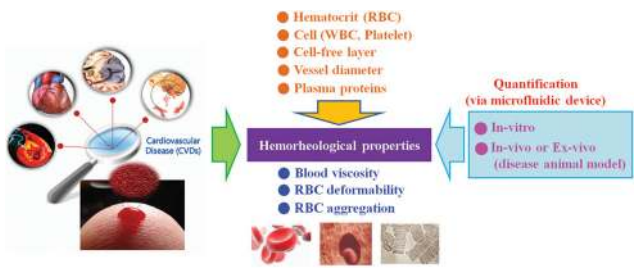

Fig. 1 Overview of quantitative measurements of haemorheological properties using microfluidic platforms and disease animal models. Haemorheological properties are determined using several factors, including haematocrit, white blood cell rheology, platelet activation, cell-free layer, vessel diameter and plasma proteins. Among them, blood viscosity, red blood cell (RBC) deformability and RBC aggregation are mainly used for the early detection of cardiovascular diseases. In this review, several measurement techniques based on microfluidic platforms (*i.e. in vitro*) or animal disease models (*i.e. in vivo* or *ex vivo*) used for quantifying haemorheological properties are categorised and discussed based on their working principles.

Microfluidic platforms possess several advantages, including small volume consumption, fast response, easy handling and disposability. Compared with conventional methods, they present a strong potential for use in point-of-care testing. Thus, microfluidic platforms have been widely used in haemorheological studies on blood. Blood viscosity can be determined by several factors, including haematocrit, plasma viscosity, RBC deformability and RBC aggregation. At high shear rates, blood viscosity is determined by the deformation and alignment of RBCs in blood flows. At low shear rates, RBC aggregation contributes to an increase in blood viscosity. In a microfluidic platform, a blood sample is delivered to a microchannel with the aid of a syringe pump. Blood viscosity is measured under stable flow conditions at shear rates higher than 10 s^{-1}.[14,15] However, at shear rates lower than the said value, a microfluidic viscometer does not provide consistent viscosity values because of unstable flow conditions. Unlike blood viscosity, RBC aggregation is quantified under quasi-static flow conditions. Specific variations in blood cells or plasma proteins are rarely employed to measure blood viscosity because blood viscosity can be determined simultaneously by several factors. Thus, the measurement of RBC deformability is fundamentally required for evaluating the mechanical properties of individual RBCs.

Three representative properties, namely, blood viscosity, RBC aggregation and RBC deformability, need to be evaluated independently when monitoring several haemorheological blood factors. In this review, several measurement techniques for haemorheological properties (blood viscosity, RBC deformability, and RBC aggregation) are categorised and discussed based on the working principles of microfluidic platforms (*i.e. in vitro*) and the use of animal disease models (*i.e. ex vivo*).

2. *In vitro* haemorheological study using microfluidic devices

2.1 Measurement of blood viscosity using a microfluidic device

Blood viscosity is the most important property for characterising blood samples.[16] As a representative biomarker, blood viscosity has been used to monitor haematological diseases effectively. It is also an essential parameter in the evaluation of wall

shear stress that acts on vascular endothelial cells.[17] Dissolved gases and nutrients are exchanged through microcirculation from narrow-sized capillary vessels to peripheral tissues and *vice versa*. Blood viscosity decreases at high shear rates due to the elongation and alignment of RBCs along the flow direction. RBCs easily pass through narrow-sized capillary vessels because the high deformability of RBCs reduces hydraulic resistance in blood vessels. However, blood viscosity increases at low shear rates due to RBC aggregation, which is significantly enhanced by several factors, including surface property of the RBC membrane, plasma proteins and haematocrit. Blood behaves as a shear-thinning fluid because blood viscosity decreases with an increase in shear rates. Haematocrit also contributes significantly to an increase in blood viscosity. Thus, blood viscosity is measured at a fixed haematocrit. Blood temperature and plasma proteins are also crucial in the measurement of blood viscosity. Blood viscosity has been clinically used in the diagnosis of haematological disorders or hyper-viscosity syndromes, including hypertension,[18,19] diabetes,[20] Alzheimer's disease,[21] stroke,[22] coronary artery disease,[23] atherosclerosis[24,25] and myocardial infarction.[26] In this section, several microfluidic-based platform techniques for evaluating fluid viscosity are reviewed and summarised in Table 1.

2.1.1 Microfluidic comparator with co-flowing streams. Quake *et al.*[27] proposed a comparator channel to measure the pressure drop in a microfluidic nonlinear resistor. The microfluidic device possessed nonlinear and control channels. Both channels were connected by a comparator channel. After supplying two fluids to the two side channels, the nonlinear relationship between the flow rate and the pressure drop was evaluated by monitoring the interface of the two fluids in the comparator channel. Stone *et al.*[28] proposed a differential manometer for measuring dynamic variations in pressure drop in a microfluidic channel [Fig. 2A-(a)]. The microfluidic device was composed of twin channels (*i.e.* test and control) connected by a comparator channel. The twin channels had rectangular cross sections (width = 5 μm and depth = 5 μm). The control fluid that flowed through the control channel was dyed to visualise the interfacial location of the two fluids in the comparator channel. A test fluid was prepared by adding RBCs to a specific solution. Using precise pressure control units, the test and control fluids were simultaneously supplied to the test and control channels, respectively. The pressure drop in the test channel changed the interfacial position between the two fluids in the comparator channel. Thus, the pressure drop in the test channel was quantified by monitoring the interfacial location in the comparator channel. The differential manometer was demonstrated to be effective in measuring the pressure drop related to the flow of RBCs, rigidified RBCs and haemolysis in the test channel.

Mugele *et al.*[29] established a unique power-law scaling relationship between interface displacement and pressure drop in a microfluidic comparator. The scaling exponent was increased from 0.51 (for a square channel) to 0.93 (for a wide

Table 1 Summary of microfluidic-based techniques for measuring fluid viscosity

Principle	Measurement quantity	Test fluid	Comment	Ref.
Co-flowing streams	Interfacial location	Non-Newtonian (PEO, CpCl-NaSal)	Image processing Conductivity measurement	31 and 33
	Interfacial location	Non-Newtonian (PEO)	Image processing Multiple shear rates	32
	Interfacial location	Non-Newtonian (PAA, PEO)	Image processing Three fluid streams	35 and 36
	Flow rate for relocating the interface to the centre channel	Newtonian (BSA)	Flow rate control with a syringe pump	37
Microfluidic flow compartment	Number of channels filled with test fluid in single microfluidic channel array	Non-Newtonian (Blood)	Digital counting Single microfluidic channel array Temperature control	14 and 38
	Number of channels filled with test fluid in 10 microfluidic channel arrays	Non-Newtonian (Blood)	Digital counting Multiple shear rates with 10 microfluidic channel arrays	39
Reversal flow switching manipulation	Flow rate for inducing reversal flow in bridge channel	Non-Newtonian (Blood)	Flow rate control with a syringe pump	15
Integrated sensor	Pressure drop at constant flow rate with a syringe pump	Non-Newtonian (Xanthan, PEO)	Bulk-sized pressure sensor MEMS pressure sensor Liquid metal-based sensor	45, 47, 48 and 49
	Flow rate at constant pressure drop	Newtonian (Monoclonal antibody)	Bulk-sized flow meter	46
Advancing meniscus	Mean velocity	Newtonian (Plasma) Non-Newtonian (Blood)	Image processing Glass or PDMS channel Self-calibration with DI water	50, 51, 53 and 54
	Flow rate under pressure control	Newtonian (BSA, Glycerin)	Smartphone-based imaging	55
	Flow rate with a hand-held pipette	Non-Newtonian (Blood)	Smartphone-based imaging Film with scale	56
Electrical impedance	Electric resistance	Newtonian (Plasma) Non-Newtonian (Blood)	Electrical impedance measurement	57

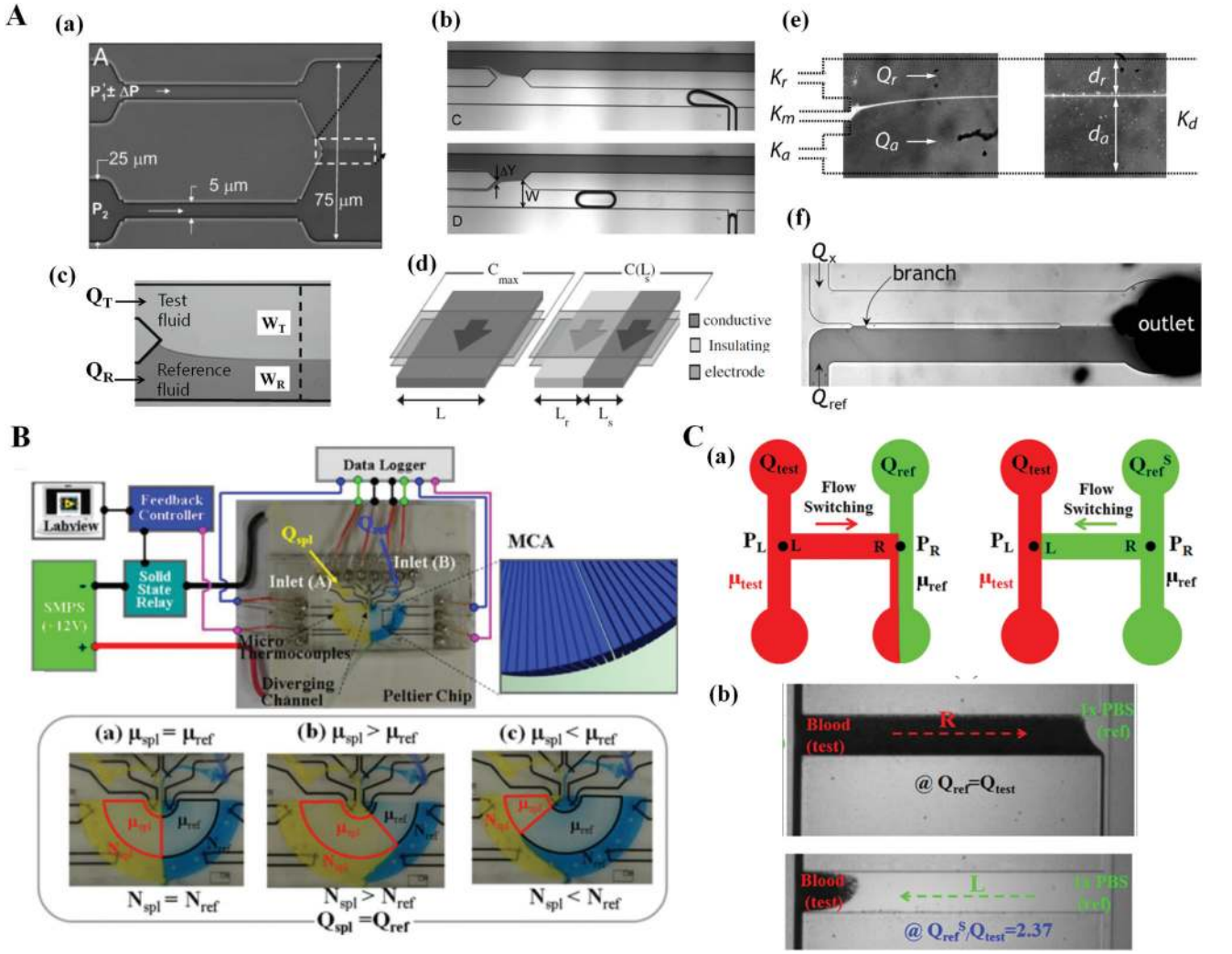

Fig. 2 Microfluidic-based viscosity measurement techniques that utilise the principles of a microfluidic comparator, a microfluidic flow compartment, and reversal flow switching manipulation. (A) A microfluidic comparator is used to measure the variations in pressure drop produced by (a) a single RBC[28] and (b) a single moving droplet.[30] (c) The fluid viscosity ratio of a test fluid to a reference fluid is quantified by monitoring the channel width (W_T, W_R) occupied by each fluid stream in a single channel.[32] (d) Interface detection by monitoring the conductivity of parallel flows between conductive and non-conductive fluids.[33] (e) Measurement of the fluid viscosity of a non-Newtonian fluid using three flowing streams.[36] (f) Interfacial relocation to the centre line by controlling the flow rate of each fluid.[37] (B) Measurement of blood viscosity by monitoring the number of channels filled with two fluids in a single microfluidic channel array.[14] (C) Measurement of blood viscosity using reversal flow switching manipulation in a Wheatstone-bridge channel.[15] (a) Flow switching manipulation in the bridge channel with varying flow rates of the reference fluid. (b) Blood flow in the bridge channel is reversely moved at a specific flow rate ratio of Q^s_{ref}/Q_{test} = 2.37. Reproduced from ref. 14, 15, 28, 30, 32, 33, 36, and 37 with permission from Springer, AIP Publishing, National Academy of Sciences, Royal Society of Chemistry, and WILEY-VCH.

channel). They integrated the microfluidic comparator into a T-junction and measured the pressure drop resulting from the confined movement of droplets in rectangular channels[30] [Fig. 2A-(b)]. Using the microfluidic comparator channel, they investigated the effects of drop size, droplet viscosity and capillary number on hydrodynamic flow resistance.

Colin *et al.*[31] utilised a microfluidic comparator to measure fluid viscosity. Parallel co-flowing streams in the microfluidic comparator (width = 200 μm and depth = 100 μm) were used [Fig. 2A-(c)]. The channel width occupied by each fluid stream depends on flow rate and fluid viscosity. Thus, the fluid viscosity of a test fluid (unknown viscosity, μ_T) with respect to the reference fluid (known viscosity, μ_R) was measured by monitoring the channel width occupied by each fluid with varying the flow rate ratio of the reference fluid to the test fluid (*i.e.* $\mu_T/\mu_R = [W_T/W_R]\cdot[Q_R/Q_T]$). The researchers used this microfluidic platform to measure the viscosities of a Newtonian fluid (oil) and a non-Newtonian fluid (PEO) for a wide range of shear rates. Compared with a conventional viscometer, the microfluidic comparator enables the measurement of fluid viscosity with a measurement accuracy of 20% error. Vanapalli *et al.*[32] proposed a multiplexed microfluidic comparator for the simultaneous measurement of fluid viscosity at various shear rates. The multiplexed microfluidic comparator was

capable of a reliable and simultaneous measurement of viscosity curves for Newtonian fluids (glycerol), polymeric solutions (PEO) and consumer products.

Colin *et al.*[33] introduced a new interface detection method with the aid of conductivity measurement without optical detection of the interface position in the microfluidic comparator [Fig. 2A-(d)]. The upper and lower electrodes were deposited on two glass substrates. A microfluidic device was prepared by bonding two glass substrates to both sides of a polymer-film channel (width = 9 mm and depth = 200 μm). During experiments, the reference fluid was used as a conductor, and the test fluid was used as an insulator. The conductivity measured by electrodes allowed for the detection of the interfacial location. This technique was applied to measure the viscosity of a non-Newtonian fluid (PEO) over a wide range of shear rates. The measured viscosity was in good agreement with that measured by a conventional rheometer, and the measurement error was within 15%. To compensate for variations in fluid viscosity depending on the interfacial location along the channel width, Kang[34] proposed the use of a correction factor (F_μ) in the viscosity formula of co-flowing streams in a rectangular channel with a certain aspect ratio (AR = depth/width) (*i.e.* $\mu_T/\mu_R = F_\mu \cdot [W_T/W_R] \cdot [Q_R/Q_T]$). Using the interfacial location obtained *via* computation fluid dynamics analysis, the correction factor was obtained as a function of interfacial location in the comparator channel. The viscosities of a Newtonian fluid (glycerin) and a non-Newtonian fluid [blood (haematocrit = 30%, 40% and 50%)] were consistently measured at various interfacial locations. Blood viscosity remained consistent regardless of the interfacial location. A quantitative study showed that the proposed method measures blood viscosity accurately and continuously.

Nguyen *et al.*[35] reported a microfluidic rheometer based on hydrodynamic focusing with three co-flowing streams. A test fluid (core stream) was sandwiched between two reference fluids (sheath flows). The width of the test fluid was varied depending on the viscosity and flow rate ratios of the test fluid to the reference fluid. The experimental results obtained for a Newtonian fluid (DI-water) and a non-Newtonian fluid (PEO) showed that the measurement range and error can be improved by adjusting the flow rate ratio between the core and sheath streams. The researchers also discovered that a microfluidic channel with a high aspect ratio is highly suitable for test fluids with a high viscosity ratio of the test fluid to the reference fluid. Meanwhile, Bausch *et al.*[36] presented a differential capillary viscometer to determine the exponent (n) of the power-law model (*i.e.* $\mu = \mu_0(\dot{\gamma})^{n-1}$, where $\dot{\gamma}$ is the shear rate) for non-Newtonian fluids (PAA and WLM) [Fig. 2A-(e)]. Unlike the microfluidic rheometer based on hydrodynamic focusing,[35] the reference fluid flowed between the two test fluids in the comparator channel. The test fluids in the reference and analyser channels experienced different shear rates in the comparator channel due to the different geometries of the reference (upper stream) and analyser (lower stream) channels. As a result, the power-law exponent determined by different geometries showed good agreement with that obtained with a conventional rheometer.

Instead of detecting the interfacial location in the comparator channel, Park *et al.*[37] used another viscosity measurement technique by adjusting the flow rate ratio to relocate the interface to the middle position of the comparator with a very small aspect ratio (*i.e.* AR = 0.047) [Fig. 2A-(f)]. When the interface was relocated to the middle position, the viscosity ratio of the test fluid to the reference fluid (μ_x/μ_{ref}) was measured by monitoring the flow rate ratio of the test fluid to the reference fluid (Q_{ref}/Q_x) (*i.e.* $\mu_x/\mu_{ref} = Q_{ref}/Q_x$). This method was successfully used to measure variations in the viscosity of a plasma protein (BSA) under various temperature conditions.

2.1.2 Microfluidic flow compartment with a microfluidic channel array. Yang *et al.*[14,38] reported a microfluidic viscometer with a microfluidic channel array (MCA) for measuring blood viscosity. Instead of detecting the interface in the comparator channel, the viscosity ratio of the test fluid to the reference fluid (μ_{spl}/μ_{ref}) was measured by counting the numbers of channels filled with each fluid at the same flow rate of both fluids (*i.e.* $\mu_{spl}/\mu_{ref} = N_{spl}/N_{ref}$). The microfluidic device was composed of two inlets and a spacious diverging channel that contains multiple identical small channels (number of channels = 89, width = 50 μm and depth = 60 μm).[14] The device was integrated with micro-scale thermocouples, a Peltier chip and a temperature controller [Fig. 2B]. Given that the proposed viscometer can measure viscosity at a single shear rate, variations in fluid viscosity over a wide range of shear rates were measured by varying the flow rate of each fluid several times. Experimental results for a Newtonian fluid (SDS) and a non-Newtonian fluid (various blood samples) indicated that the normalised difference between the proposed method and a conventional viscometer was less than 5%. By contrast, to generate multiple shear rate conditions (*i.e.* 10 different shear rates) at a single flow rate, Yang *et al.*[39] proposed a microfluidic viscometer with 10 MCAs (the total number of each microfluidic channel array = 100). Each microfluidic channel array had different channel widths. The proposed method could measure variations in blood viscosity for at least 10 different shear rates. Compared with the normalised difference of conventional viscometers, that of the proposed method was approximately 5.3%.

2.1.3 Manipulation of reversal flow switching in a Wheatstone-bridge channel. Lee *et al.*[15] measured fluid viscosity by monitoring reversal flow switching in the microfluidic analogue of a Wheatstone-bridge circuit. The microfluidic device was composed of two sets of inlets and outlets, two identical side channels for guiding two fluids and one bridge channel connected to the side channels. Flow switching in the bridge channel was caused by hydrodynamic force balancing at both junctions of two side channels. When the viscosity of a test fluid (μ_{test}) is larger than that of the reference fluid (μ_{ref}) at the same flow rate ($Q_{test} = Q_{ref}$), the test fluid moves in the right direction in the bridge channel because the pressure at the left junction is higher than that at the right junction ($P_L > P_R$). To obtain a hydrodynamic balance between both side channels, the flow rate of the reference fluid was precisely controlled to increase pressure at the right junction. The flow

direction of the reference fluid was reversed towards the left direction at a specific flow rate ratio (Q^S_{ref}/Q_{test}). Then, the viscosity ratio of the test fluid to the reference fluid was measured by monitoring the specific flow rate ratio (*i.e.* $\mu_{test}/\mu_{ref} = Q^S_{ref}/Q_{test}$) [Fig. 2C-(a)]. To demonstrate the performance of the proposed method, blood with haematocrit = 50% (test fluid) and 1× PBS (reference fluid) were simultaneously supplied to each inlet of the microfluidic device by using two syringe pumps. At a specific flow rate ratio of $Q^S_{ref}/Q_{test} = 2.37$, the test fluid reversely flowed from the right direction (*i.e.* $Q_{test} = Q_{ref}$) to the left direction in the bridge channel. By monitoring the reversal flow switching in the bridge channel, the viscosity ratio of the test blood to the reference fluid was quantified as $\mu_{test}/\mu_{ref} = 2.37$ [Fig. 2C-(b)]. The proposed method was then employed to measure the viscosity of Newtonian fluids (glycerin and oil). The normalised difference in viscosity measured by the proposed method was 6.5% less than that obtained by a conventional method. In addition, blood viscosity was successfully measured for blood samples with different haematocrit, RBC membrane fixation and channel width of both side channels. This reversal flow switching method was successfully utilised to evaluate the relationship between velocity profile and blood viscosity[40] and measure the blood viscoelasticity[41] and blood viscosity of blood circulating in a rat bypass loop.[42–44]

2.1.4 Integrated sensor-based measurement of fluid viscosity. Using the pressure drop measured by a pressure transducer installed in the microfluidic channel (width = 150 μm and depth = 150 μm),[45] the fluid viscosity at a specific flow rate has been estimated using the Hagen–Poiseuille equation (*i.e.* pressure drop (ΔP) = fluidic resistance [R_f]·flow rate [Q]). To evaluate polymer degradation, the viscosity of a PEO solution as a non-Newtonian fluid was measured at a high shear rate of 10^6 s^{-1}.

Migler *et al.*[46] used a micro-capillary viscometer to characterise the kinematic behaviour of protein solutions. The viscometer consisted of two pressure chambers connected by a polyethylene tube *via* an external flow rate meter. By measuring the flow rate under precise pressure-difference control, the viscosity of a test fluid was evaluated *via* an analytical formula. The micro-capillary viscometer was used to measure the viscosity of a monoclonal antibody as a function of the shear rate, protein concentration and temperature.

To measure the pressure drop in a microfluidic channel using three integrated pressure sensors, McKinley *et al.*[47] utilised a high-shear-rate viscometer to measure the viscosity of complex fluids at a high shear rate of 80 000 s^{-1}. The microfluidic device was fabricated from Pyrex mounted on a gold-coated silicon with MEMS-based pressure sensors (width = 800 μm and depth = 800 μm). Similarly, Ayela *et al.*[48] used a capillary rheometer to measure the viscosity of silicon oil over a broad range of shear rates. The viscometer was composed of an anodic bonded silicon–Pyrex derivative microfluidic channel equipped with local electrodes [Fig. 3A-(a)].

Yang *et al.*[49] used a liquid metal-based pressure sensor [Fig. 3A-(b)]. The integrated pressure sensor in the microfluidic device was composed of three polydimethylsiloxane (PDMS) layers, namely, a microfluidic channel for fluid flow (lower layer), a thin film (separation layer) and an electrical-resistance channel (upper channel). The electrical-resistance channel was filled with Galinstan as a liquid metal. The pressure that developed in the microfluidic channel decreased the cross-sectional area of the electrical-resistance channel, which in turn led to an increase in electrical resistance. The pressure at a specific position in the microfluidic channel was evaluated by measuring the variations in electric resistance. The variations in electrical resistance were determined for given pressure conditions by using an analogue circuit that included a Wheatstone-bridge circuit and an operational amplifier. To use the liquid metal-based pressure sensor, its calibration curve was obtained by varying the pressure from 0 kPa to 230 kPa for deionized water. The viscosity of a test fluid that flowed through a microfluidic channel with a rectangular shape was estimated by using the Hagen–Poiseuille relation for a specific flow rate. The proposed method was applied to measure the viscosities of a Newtonian fluid (SDS) and a non-Newtonian fluid (PEO). The normalised difference between the proposed method and a conventional viscometer was less than 7%.

2.1.5 Advancing meniscus in a single capillary channel. Burns *et al.*[50,51] used a self-calibrated microfluidic capillary viscometer to measure fluid viscosity with a capillary force-driven flow. The capillary viscometer was created by bonding a glass channel to a silicon substrate. The glass channel was etched to have a rectangular cross-sectional shape (width = 340 μm, depth = 35 μm) [Fig. 3B-(a)]. When a small drop of liquid (0.6 μL) was placed at the inlet of the microfluidic channel, the difference in the advancing meniscus (R_2) and the receding meniscus (R_1) induced a capillary pressure difference. This capillary pressure difference made the liquid move as time elapsed [Fig. 3B-(b)]. An analytical study indicated that fluid viscosity (μ) can be determined as functions of surface tension, contact angle and channel geometry. In other words, prior knowledge of surface tension, contact angle and channel geometry is required to evaluate fluid viscosity. In addition, variations in surface tension, contact angle and channel geometry can reduce measurement accuracy. To solve these problems, a self-calibrated microfluidic viscometer comprising two identical parallel channels was recommended. The recommended viscometer could accurately measure the viscosity of test fluids by eliminating the effects of surface tension, contact angle and channel geometry on measurement accuracy. In a demonstration, the viscosities of biofluids (urine and blood plasma) as Newtonian fluids were accurately measured with a 3% error compared with a conventional viscometer.[50] The self-calibrating viscometer could also accurately measure the viscosity of non-Newtonian fluids, including PEO, xanthan gum and hydrolysed polyacrylamide.[51] Furthermore, the viscosity of a test fluid was automatically measured by monitoring the advancing meniscus in the channel through the use of three droplet sensing techniques, namely, a digital electrode, an analogue electrode and a thermal electrode.[52]

To replace expensive silicon-glass devices, Zheng *et al.*[53,54] introduced a PDMS viscometer for monitoring the advancing

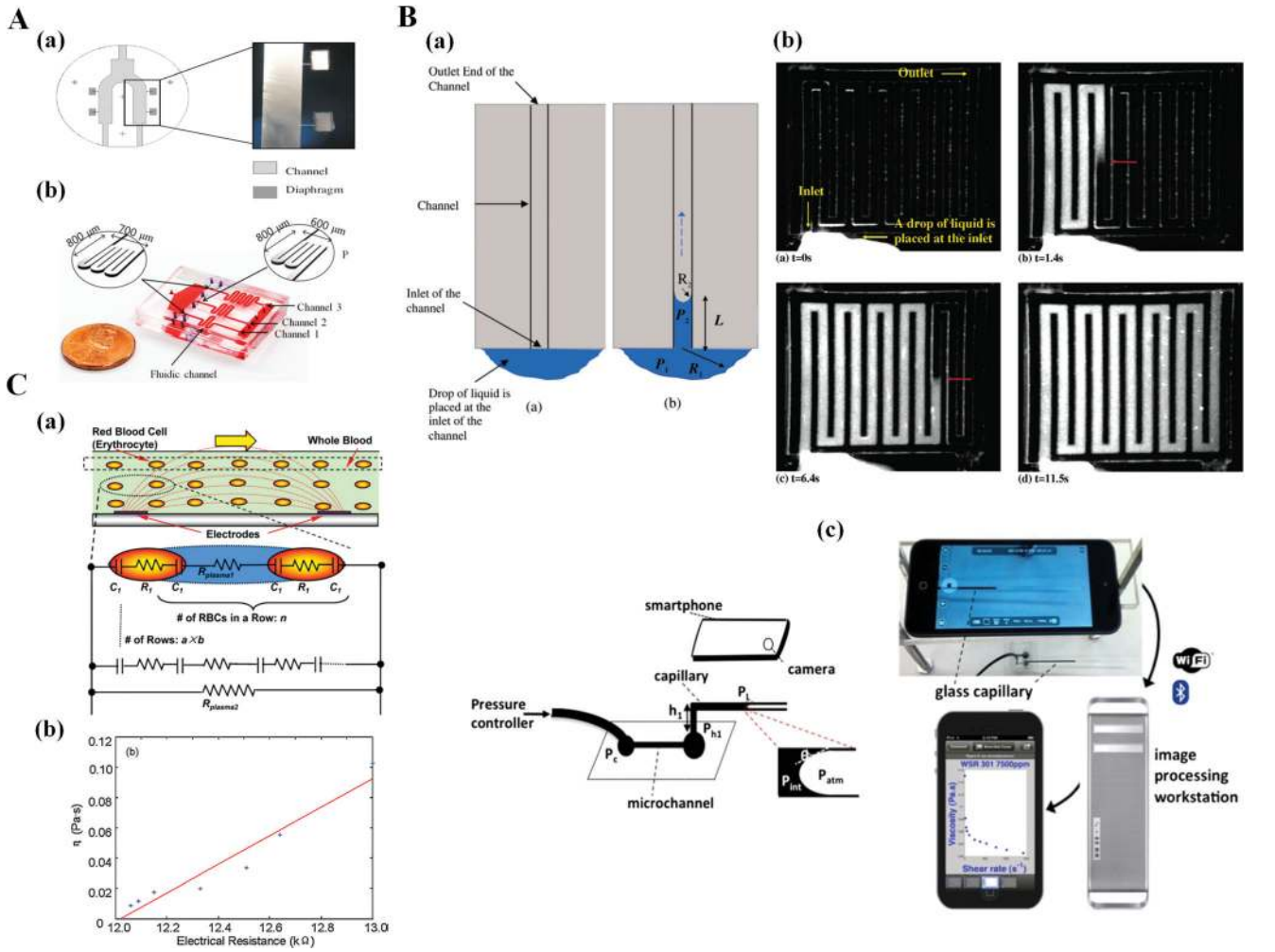

Fig. 3 Microfluidic-based viscosity measurement techniques that utilise the principles of an integrated sensor, an advancing meniscus and electrical impedance. (A) Measurement of fluid viscosity using an integrated sensor. Under a given flow rate condition, the pressure drop is measured using (a) a membrane deflection-based pressure sensor[48] and (b) a liquid-metal-based pressure sensor.[49] (B) Measurement of fluid viscosity using an advancing meniscus in a single capillary channel. (a) A capillary viscometer using a capillary force-driven flow.[50] (b) Snapshot showing the advancing meniscus of a test fluid over time.[50] (c) A stress-controlled microfluidic viscometer combined with a smartphone.[55] (C) Measurement of blood viscosity using electrical impedance spectroscopy.[57] (a) Equivalent circuit model of blood flow. (b) Relationship between electric resistance and apparent viscosity. Reproduced from ref. 48–50, 55, and 57 with permission from Springer, AIP Publishing, MDPI AG, American Chemical Society and Elsevier Science SA.

meniscus of a test liquid in a capillary channel. The wettability of the fluid on the PDMS surface did not affect the viscosity measurement because the capillary forces were cancelled out in the data analysis. For various fluids, including Newtonian fluids (*i.e.* glycerin, blood plasma and ethanol)[53] and non-Newtonian fluids (*i.e.* PEO and blood),[54] the PDMS-based viscometer measured the fluid viscosity more consistently than conventional viscometers.

Instead of a capillary pressure-driven flow in the capillary channel, Vanapalli *et al.*[55] developed a stress-controlled microfluidic viscometer with the aid of a smartphone [Fig. 3B-(c)]. The flow rate of a test fluid was measured by monitoring the advancing interfacial motion in a glass capillary. Fluid was continuously supplied to a microfluidic channel (width = 1000 μm and depth = 31 μm) by using a constant pressure source. A smartphone was utilised to visualize the advancing meniscus of the fluid in the glass capillary attached to the outlet of the microfluidic channel. By analysing the interface movement in the glass capillary from images captured by the smartphone, the viscosity of the test fluid was determined using the analytical formula between pressure drop and flow rate. Unlike previous methods, this approach enables the measurement of the viscosity of multiple samples in parallel because all samples can be supplied by a single pressure source. For a typical demonstration, the proposed method was used to measure the viscosities of Newtonian fluids (glycerin and BSA) and a non-Newtonian fluid (PEO). Instead of an external pressure source, a handheld pipette was used to simultaneously supply blood and the reference fluid into parallel capillary channels.[56] By using a quantification method similar

to that proposed by Vanapalli *et al.*,[55] the researchers measured blood viscosity over various shear rates.

2.1.6 Electric impedance-based blood measurement. Zhao *et al.*[57] examined the rheological properties of blood in a microfluidic channel. The rheological behaviour of blood was evaluated by measuring electrical impedance (resistor and capacitor) *via* electrical impedance spectroscopy. As illustrated in Fig. 3C-(a), blood was modelled as a discrete circuit network. An individual RBC was represented by two capacitors and one resistor connected in series.[58] However, blood plasma was only modelled as a resistor. Two microelectrodes (width = 500 μm, thickness = 0.5 μm and interspace = 500 μm) were patterned on the bottom surface of the microchannel (width = 500 μm and depth = 500 μm). The electrodes were extended over the entire width of the microfluidic channels. The electrical impedance of blood flow was measured by sweeping the stimulating frequency in the range of 1 Hz to 100 kHz. The electrical resistance of blood plasma remained constant over a wide range of shear rates. The electrical resistance varied by less than 2%. Fig. 3C-(b) shows the relationship between electrical resistance and fluid viscosity. Regression analysis of the relationship between blood viscosity and electrical resistance revealed a high correlation coefficient (*i.e.*, R^2 = 0.935). Thus, the electrical impedance-based rheometer has potential for use in determining the rheological properties of blood samples.

2.1.7 Discussion on blood viscosity techniques. As summarised in Table 1, several measurement techniques have been developed to measure the shearing viscosity of various Newtonian or non-Newtonian fluids. The microfluidic flow compartment method, the reversal flow switching manipulation method and the co-flowing stream method can measure the viscosity of various blood specimens over a wide range of shear rates. First, the microfluidic flow compartment method can measure blood viscosity by counting the number of channels filled with blood in a label-free and sensor-less manner. However, the measurement accuracy of the method decreases when many channels are filled with blood (*i.e.* high viscosity ratio of blood to the reference fluid). In addition, clogging of cells and bubbles (air or oxygen) hinders the accurate measurement of blood viscosity.[59] Two precise syringe pumps are required to control two fluids at constant flow rates. Image acquisition with a microscope or a high-speed camera is also required to count the number of channels filled with blood.

Second, the reversal flow switching manipulation method can monitor the reversal of flow direction by varying the flow rate of the reference fluid using a syringe pump. Measurement accuracy depends largely on the performance of the syringe pump. An air compliance unit[60] is adopted to consistently deliver blood and reference fluid at consistent flow rates. Critical issues, including clogging of cells and the presence of bubbles, can be minimised using a simple H-shaped channel. Compared with the microfluidic flow compartment method, the reversal flow switching manipulation method can evaluate blood viscosity within a specific duration of time. However, difficulties arise when this method is used to continuously measure blood viscosity.

The co-flowing stream method can be considered a promising alternative for measuring blood viscosity in a continuous and label-free manner. Given that this method adopts a wide rectangular channel with a very small aspect ratio, critical issues, including clogging of cells and the presence of bubbles, can be resolved. Furthermore, when two syringe pumps are removed using a hand-held pipette[56] or an air-compressed syringe,[61] the method might present a high potential for use in clinical settings. If the co-flowing stream method includes a correction factor (*i.e.* a modified parallel flow method),[62] blood viscosity could be measured reliably and continuously under *ex vivo* conditions.

2.2 Measurement of RBC deformability using a microfluidic device

Given that the characteristic length scale of a microfluidic channel is similar to that of cells, a microfluidic device is considered a promising platform for probing mechanical biomarkers.[63] Compared with conventional biochemical biomarkers, the mechanical biomarkers in a microfluidic device possess several advantages, including being label-free, high throughput and potential cost-effectiveness. Various approaches, including micropipette aspiration, cell transit analysis, optical stretching and atomic force microscopy, have been recommended to measure the mechanical properties (*i.e.* viscoelasticity, Young's modulus and viscosity) of individual cells.[64] Blood viscosity significantly varies depending on several factors, including haematocrit, plasma proteins, RBC deformability and RBC aggregation. Therefore, changes in individual RBCs are not effectively detected by measuring blood viscosity. RBC deformability has recently elicited considerable attention as an effective means of evaluating variations in individual RBCs. RBC deformability is determined by several factors, such as membrane cytoskeleton, membrane integral proteins, cytoplasmic viscosity and the ratio of surface area to volume.[65] Given their high deformability, normal RBCs easily pass through a narrow-sized capillary. However, the membrane flexibility of each RBC is reduced because of cytoskeleton disorders, invasion of cancer cells and activation of antigens.[64] A slight decrease in RBC deformability results in increased blood viscosity and fluidic resistance in the microvasculature. Thus, RBC deformability can be utilised as a promising biomarker for detecting various haematological disorders, including malaria, sepsis, diabetes and sickle cell anaemia. In addition, it has a high potential for detecting biological heterogeneity and inherent variations in cell populations. This section focuses on several techniques that can characterise RBC deformability by using microfluidic platforms. Several methods for measuring RBC deformability using microfluidic platforms are summarised in Table 2.

2.2.1 Cell blockage in microfluidic channels. To characterise the dynamic behaviours of individual cells, a microfluidic device was used in a previous study to examine multicellular

Table 2 Summary of microfluidic-based techniques for measuring RBC deformability

Principle	Measurement quantity	Test cell	Comment	Ref.
Cell blockage	Minimum cylinder diameter (MCD)	Malaria-infected RBCs	Tapered channel Single cell Low throughput	68
	Clogging	Malaria-infected RBCs	Single channel	66
		Hardened RBCs	Capillary network	67
		Monocytic THP-1	Gradual filters Low throughput	69
Cell aspiration	Young's modulus (aspiration length)	Lung tumours (A549, 95C)	Straight channel	70
	Cortical tension	Malaria-infected RBCs	Funnel-shaped channel	71
Cell transit	Deformability index	RBC, WBC	Hyperbolic converging channel	73
	Cell margination	Malaria-infected RBCs	Single channel	74
	Transit time	RBC, neutrophil HL60 myeloid leukemia	Parallel capillary network	75
	Entry time, flow speed and cell deformation	K562 leukemia	Parallel micro-sized constriction	76 and 77
	RBC velocity	Hardened RBCs	Capillary network	79
	RBC velocity	Malaria-infected RBCs	Triangular-shaped pillar channels	78
	Cell lysis	Hardened RBCs	Four filters with different orifice lengths	80
	Deformability-based sorting	Malaria-infected RBCs RBC, WBC, CTC	Microfluidic with tapered channels High throughput	55 and 81
	Blood velocity Image intensity	Malaria-infected RBCs Hardened RBCs	Multiple micro pillars High throughput Constant or pulsatile blood flow	62, 65 and 83
Optical stretcher	Cell elongation	Malaria-infected RBCs	Strain model with Kelvin-Voigt model Low throughput	84
Electric impedance	Transit time Impedance (magnitude, phase)	RBC, WBC	Single cell	86
	Impedance (magnitude, phase)	Malaria-infected RBCs	Single cell Low throughput	85

capillary blockages.[66] Fig. 4A-(a) shows the microfluidic channel with a constricted segment. Normal RBCs passed through a 2 μm constriction. However, malaria-infected RBCs (*i.e.* schizont form) were blocked by a 6 μm constriction. This result implies that a microfluidic device can be used as an analytical tool to investigate the dynamic behaviours of RBCs under capillary-flow conditions.

As illustrated in Fig. 4A-(b), RBCs with impaired deformability were blocked in capillaries. Wang *et al.*[67] used a discrete circuit model to analyse variations in physical properties in capillaries caused by the clogging of RBCs. Experimental demonstrations and theoretical analysis demonstrated that the microfluidic capillary network can effectively measure RBC deformability.

Rathod *et al.*[68] suggested the concept of minimum cylinder diameter (MCD) for determining the filterability of individual RBCs in microfluidic channels. As shown in Fig. 4A-(c), individual RBCs were trapped in wedge-shaped microfluidic channels. Then, MCD was calculated from the surface area and volume of RBCs trapped in the channels. The histogram of MCD measurement data indicated a distinctive difference between malaria-infected RBCs (*i.e.* MCD = 3.26 ± 0.32 μm) and normal RBCs (*i.e.* MCD = 2.64 ± 0.17 μm). The result showed that the MCD calculated from the surface area and volume of the RBCs trapped in the microfluidic channels can be effectively used to distinguish malaria-infected RBCs.

Theodoly *et al.*[69] presented a microfluidic gradual filter for separating cells by using cell deformability. As shown in Fig. 4A-(d), the microfluidic filter was composed of two different heights (*i.e.* blue for 14 μm and red for 4 μm). The cross section of the filter channel was along the flow direction. When cells entered the gradual filter, the red-labelled rigid cells and green-labelled normal cells were distinctively separated. The cells trapped in the gradual filter were clearly separated by cell stiffness (or deformability) at a low throughput of 100 cells per injection.

2.2.2 Cell aspiration in microfluidic channels. Yue *et al.*[70] proposed the use of instantaneous Young's modulus ($E_{\text{instantaneous}}$) for characterising single cells in suspension. As shown in Fig. 4B-(a), a single cell was aspirated continuously in a straight constriction channel, and the cellular entry process was monitored with a high-speed camera. Microscopic images showed the cellular entry process into the constriction channel, including (stage I) instantaneous jumping into the channel that can be quantified by instantaneous aspiration length ($L_{\text{instantaneous}}$), (stage II) a gradual increase in aspiration length and (stage III) transitional position represented by transitional aspiration length ($L_{\text{transitional}}$). Numerical analysis showed that the aspiration lengths ($L_{\text{instantaneous}}$ and $L_{\text{transitional}}$) were reversely proportional to instantaneous Young's modulus. Using this method, the $E_{\text{instantaneous}}$ of two lung tumour cells, A549 and 95C, was measured. As depicted

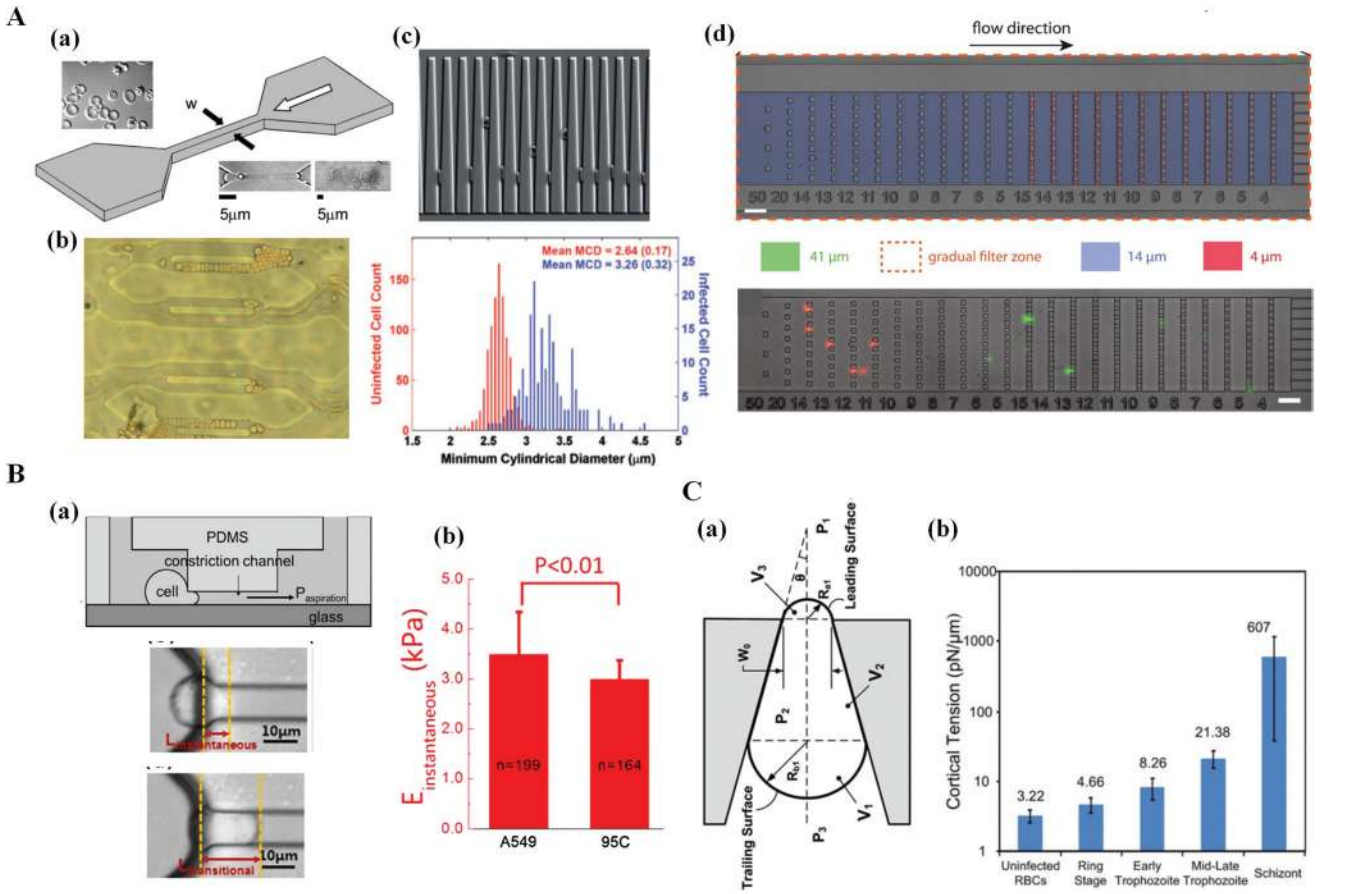

Fig. 4 Measurement of RBC deformability using clogging, instantaneous Young's modulus, and cortical tension. (A) Cell blockage in capillary channels: (a) clogging in a single-constriction capillary,[66] (b) clogging in capillary networks,[67] (c) the minimum cylinder diameter of cells trapped in taper channels[68] and (d) clogging in gradual filters with variable pore sizes.[69] (B) Instantaneous Young's modulus ($E_{instantaneous}$) estimated using transitional aspiration length in the constriction channel.[70] (a) Cell entry process into a constriction channel. (b) Quantification of $E_{instantaneous}$ for A549 cells (n = 199) and 95C cells (n = 164). (C) Variation in cortical tension for uninfected and malaria-infected RBCs.[71] (a) Cortical tension is analytically determined from deformed RBCs in a funnel-shaped constriction. (b) Variations of cortical tension with respect to each stage of the parasitized cell. Reproduced from ref. 66–70, and 71 with permission from the National Academy of Sciences, Springer, WILEY-Blackwell, Royal Society of Chemistry, and Elsevier Science SA.

in Fig. 4B-(b), the value of $E_{instantaneous}$ was 3.48 ± 0.86 kPa for A549 cells (n = 199) and 2.99 ± 0.38 kPa for 95C cells (n = 164). The $E_{instantaneous}$ values of A549 and 95C showed significant differences (*i.e.* $P < 0.01$). This result showed that instantaneous Young's modulus can be used to characterise the biophysical properties of individual cells.

Ma *et al.*[71] used cortical tension to detect malaria-infected RBCs. The microfluidic device was composed of two layers, namely, a fluidic channel with multiple funnel-shaped constrictions[72] and a pressure attenuator. They also used the asymmetric ratchet structure to study the directional mobility of cells.[72] Using a geometric model of RBC squeezed through the funnel constriction as depicted in the inset of Fig. 4C-(a), the relationship between pressure difference ($\Delta P = P_3 - P_1$) and cortical tension (T_c) was analytically derived as $\Delta P = T_c(1/R_{a1} - 1/R_{b2})$. R_{a1} was equal to $W_0/2$. R_{b1} can be calculated based on mass conservation between the undeformed normal cell and the squeezed cell in the funnel channel. As shown in Fig. 4C-(b), the cortical tension at each stage of the parasitized cell was evaluated as 3.22 ± 0.64 pN μm^{-1} (uninfected), 4.66 ± 1.15 pN μm^{-1} (ring stage), 8.26 ± 2.84 pN μm^{-1} (early-trophozoite stage), 21.38 ± 5.81 pN μm^{-1} (mid-late trophozoite stage) and 607 pN μm^{-1} (schizont stage). The malaria-infected RBCs from ring stage to schizont stage were 1.5 to 200 times stiffer than uninfected normal RBCs. Thus, the cortical tension of individual RBCs can be effectively used to detect each infection stage of malaria-infected RBCs.

2.2.3 Cell transition in microfluidic channels. Lima *et al.*[73] proposed an integrative microfluidic device for simultaneously separating the RBCs and WBCs of blood samples and for assessing their deformability indices. By streaming WBCs or RBCs through a converging hyperbolic channel with sudden expansion, the major-axis (L_{major}) and minor-axis (L_{minor}) lengths of each cell were measured to determine the deformability index (DI), namely, DI = ($L_{major} - L_{minor}$)/($L_{major} + L_{minor}$). As illustrated in Fig. 5A, both cells (n = 169)

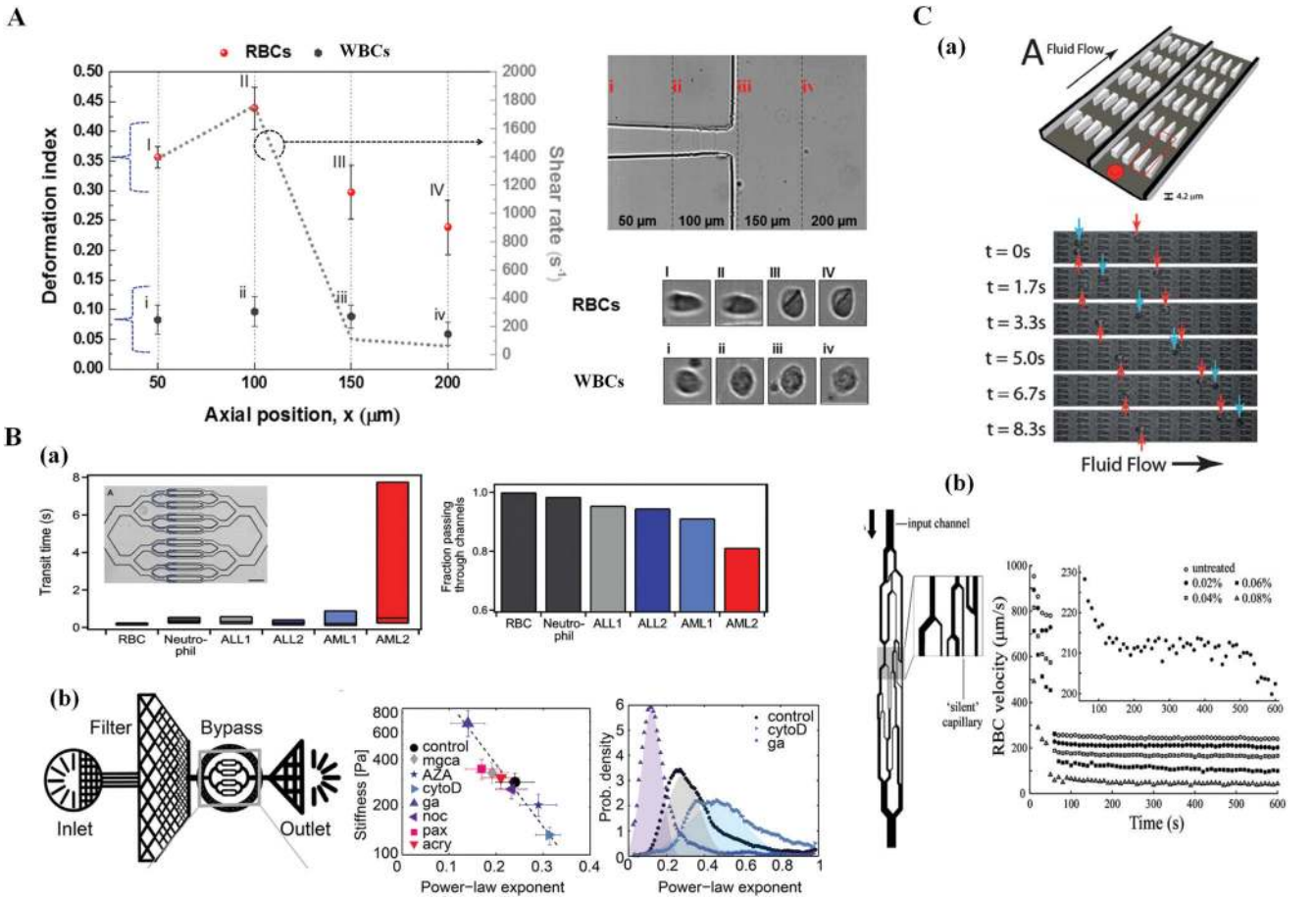

Fig. 5 Measurement of RBC deformability using the deformability index, transit time and velocity of individual RBCs. (A) Variations in the deformability index of RBC and WBC flowing along the axial position in a hyperbolic converging microchannel.[73] (B) Transit time of individual RBCs passing through a capillary network. (a) Variation in single-cell transit time and occlusion at different disease states.[75] (b) Measurement of cell fluidity (β) and stiffness (E) for quantifying the mechanical properties of cells in suspension: the microfluidic device (top), inverse relationship between stiffness (E) and power-law exponent (β) (lower left) and distribution of β for cell deformability (lower right).[76] (C) Velocity measurement of individual RBCs for detecting (a) malaria-infected RBCs[78] and (b) impaired deformability of RBCs.[79] Reproduced from ref. 73, 75, 76, 78, and 79 with permission from Springer, Royal Society of Chemistry, and Cell Press.

had the maximum value of DI (DI_{max}) at the axial position of 100 μm in the converging channel (*i.e.* DI_{max} = 0.10 for WBCs and DI_{max} = 0.44 for RBCs), where the average shear rate had the maximum value of 1761.6 s^{-1}. In addition, the deformability of RBCs was much higher than that of WBCs. Thus, the proposed method can be used to simultaneously separate blood cells and assess the deformability of individual cells.

Lim *et al.*[74] used deformation-based cell margination for separating malaria-infected RBCs from blood samples. The randomly distributed malaria-infected RBCs (*i*RBCs) at the inlet channel move towards the sidewalls as blood passes through a long straight microfluidic channel (width = 15 μm, depth = 10 μm and length = 30 mm). For a demonstration, blood infected with ring and late trophozoite–schizont *i*RBCs (haematocrit = 40%) was supplied to the inlet channel at a flow rate of 5 μL min^{-1}. The separation performance of the device was evaluated by conducting flow cytometry analysis at the outlet channels. The experimental results indicated a high filtration efficiency of 92% for late trophozoite–schizont *i*RBCs and 75% for early ring *i*RBCs. Thus, cell margination can be used to separate *i*RBCs based on the deformability of individual RBCs.

To enhance the throughput of the flow cytometry technique, Fletcher *et al.*[75] utilised single-cell transit time elapsed for passing through capillary networks. As shown in the inset of Fig. 5B-(a), the flow cytometry device was trifurcated into two wide bypass channels and a network of bifurcating channels split into 64 parallel capillaries (width = 5.89 μm, depth = 13.3 μm and length = 130 μm). To characterise biophysical properties at different disease states, variations in single-cell transit times were measured using flow cytometry for blood cells collected from an acute myeloid leukaemia (AML) patient with leukostasis symptoms (AML_2), an AML patient without leukostasis symptoms (AML_1) and two ALL patients without leukostasis symptoms (ALL_1 and ALL_2). Neutrophils and RBCs were also collected from a healthy volunteer. As illustrated in Fig. 5B-(a), the cell transit time and occlusion were signifi-

cantly increased for disease states compared with those in the control case. The transit time was significantly reduced by administrating drugs for the cells collected from patients with leukostasis symptoms. Thus, the transit time of single cells can be used to assess the biophysical properties of blood cells with the benefit of high throughput.

Fabry *et al.*[76,77] suggested the concept of cell fluidity (β) for quantifying the mechanical properties of cells in suspension. As shown in Fig. 5B-(b), the microfluidic device was composed of inlet, debris filter and eight parallel constrictions (width = 5 μm and depth = 9 μm) surrounded by a bypass and an outlet. By measuring the driving pressure (ΔP), maximum shear strain (ε_{max}) and entry time (t_{entry}) of cells in the microfluidic constrictions, the cell stiffness (E) and power-law exponent (β) were estimated *via* the power-law relationship of $t_{entry} = (\varepsilon_{max}E/\Delta P)^{1/\beta}$. The experimental results for K562 leukaemia cells showed an inverse relationship between cell stiffness (E) and the power-law exponent (β). Given that the power-law exponent (β) represents cell fluidity, it was only used to compare the mechanical properties of individual cells for control, cells treated with cytochalasin D and cells treated with glutaraldehyde solution. As a result, β had significantly different values ($\beta = 0.31 \pm 0.12$ for control, $\beta = 0.45 \pm 0.15$ for cytochalasin D and $\beta = 0.17 \pm 0.04$ for glutaraldehyde).[76] Furthermore, to examine the mechanical response of cells to protein expression levels,[77] the researchers simultaneously measured the mechanical properties (E and β) and fluorescence signals of individual cells by using protein lamin A. Cell stiffness (E) was increased and cell fluidity was decreased as the level of lamin A increased. Therefore, the suggested method can be used for quantitative high-throughput measurement (*i.e.* 10 000 cells per hour) of cell mechanical properties with a microfluidic device.

Han *et al.*[78] employed a cell velocity-based cytometer to detect malaria-infected RBCs in a microfluidic device with periodically spaced and triangle-shaped pillars (entrance space = 3 μm and depth = 10 μm). As shown in Fig. 5C-(a), the microfluidic device was composed of 10 pillars laterally and 200 pillars longitudinally. Microscopic images indicated differences in cell velocities for ring stage *P. falciparum*-infected RBCs (red arrow) and normal RBCs (blue arrow). After 8.3 s, the moving velocity of normal RBCs was two times faster than that of malaria-infected RBCs. The proposed method was able to analyse the deformability of approximately 10 000 RBCs before significant clogging occurred in the microfluidic device.

Bitensky *et al.*[79] used RBC velocity for the direct measurement of the impaired deformability of RBCs in microvascular networks. As shown in Fig. 5C-(b), the microfluidic network was composed of 34 microchannels (width = 6–70 μm and depth = 6 μm). The experimental results indicated that RBC velocity was significantly decreased by the increase in the concentration of glutaraldehyde solution from 0% (control) to 0.08%. Network perfusion depended on RBC deformability and had high sensitivity to small variations in deformability.

Cho *et al.*[80] used the cell lysis rate as a function of the areal strain (ε_A) of a cell membrane to monitor the deformability of individual RBCs. As shown in Fig. 6A-(a), the microfluidic device comprised four filters with different orifice lengths (width = 2 μm, depth = 2.2 μm and length = 2–16 μm) connected in series along the microfluidic channel. An electric circuit was integrated to digitally count the number of individual RBCs passing through the four filters. Using normal RBCs and chemically hardened RBCs with 0.5 mM azodicarboxylic acid, accumulated lysis rates were measured with varying orifice lengths. As shown in Fig. 6A-(b), a significant difference in lysis rate was found at the orifice length (L) (*i.e.* L = 4.3 and 6.7 μm). The experimental results showed that $\varepsilon_A = 0.15$ was effective in discriminating deformability differences between normal and hardened RBCs. In addition, the deformability of individual RBCs can be monitored at a rate of 400 cells per minute.

To effectively diagnose malaria-infected RBCs, Ma *et al.*[81] proposed a simple method for sorting RBCs based on deformability and enriching the concentration of ring-stage *P. falciparum*-infected RBCs. As shown in Fig. 6B-(a), deformability-based sorting of RBCs was conducted by using oscillatory flow around asymmetric ratchet constrictions (width = 1.5 to 7.5 μm and depth = 4.5 μm). As shown in Fig. 6B-(b), hardened RBCs exposed to 0% to 0.01% glutaraldehyde solution were collected from outlets 1 to 3. Cell distribution shifted rightwards with the increase in the concentration of the glutaraldehyde solution from 0.015% to 0.05%. To investigate the enrichment of ring-stage malaria-infected RBCs with low parasitemia, the researchers prepared and collected blood samples with parasitemia ranging from 0.0004% to 0.04% from outlets 4 to 7. As shown in Fig. 6B-(c), samples with a starting parasitemia level order that was lower than the detection limits of microscopy were enriched to a detectable range. Furthermore, the proposed method was applied to detect circulating tumour cancer cells,[82] and the method captured >90% of cancer cells from unprocessed whole blood with 10^4-fold enrichment of target cells.

Lee *et al.*[83] evaluated RBC deformability by measuring blood velocity and the image intensity of blood flow in a microfluidic channel array (N = 105, minimum gap = 2 μm and depth = 10 μm), as shown in Fig. 6C-(a). To effectively detect the difference in the subpopulation of RBCs, the air compliance effect was considered by adding a cavity of approximately 0.3 mL over 0.2 mL blood (haematocrit = 50%) in a disposable syringe (1 mL). Based on the transient behaviour of blood flows, RBC deformability was estimated by using three parameters [minimum value of blood velocity ($\langle U \rangle_{min}$), blood volume (ΔV) and clogging index (C.I.)]. The proposed method was applied to measure the RBC deformability of homogeneous blood, heterogeneous blood and malaria-infected RBCs. As a result, the three selected parameters were significantly varied depending on the degree of deformability. Deformability measurement of blood samples (0.2 mL, 50% haematocrit) was completed within 10 min. Furthermore, to monitor variations in haemodynamic factors, the deformability and viscosity[65] (or viscoelasticity[62]) of blood samples were evaluated by quantitatively visualising blood flows in a micro-

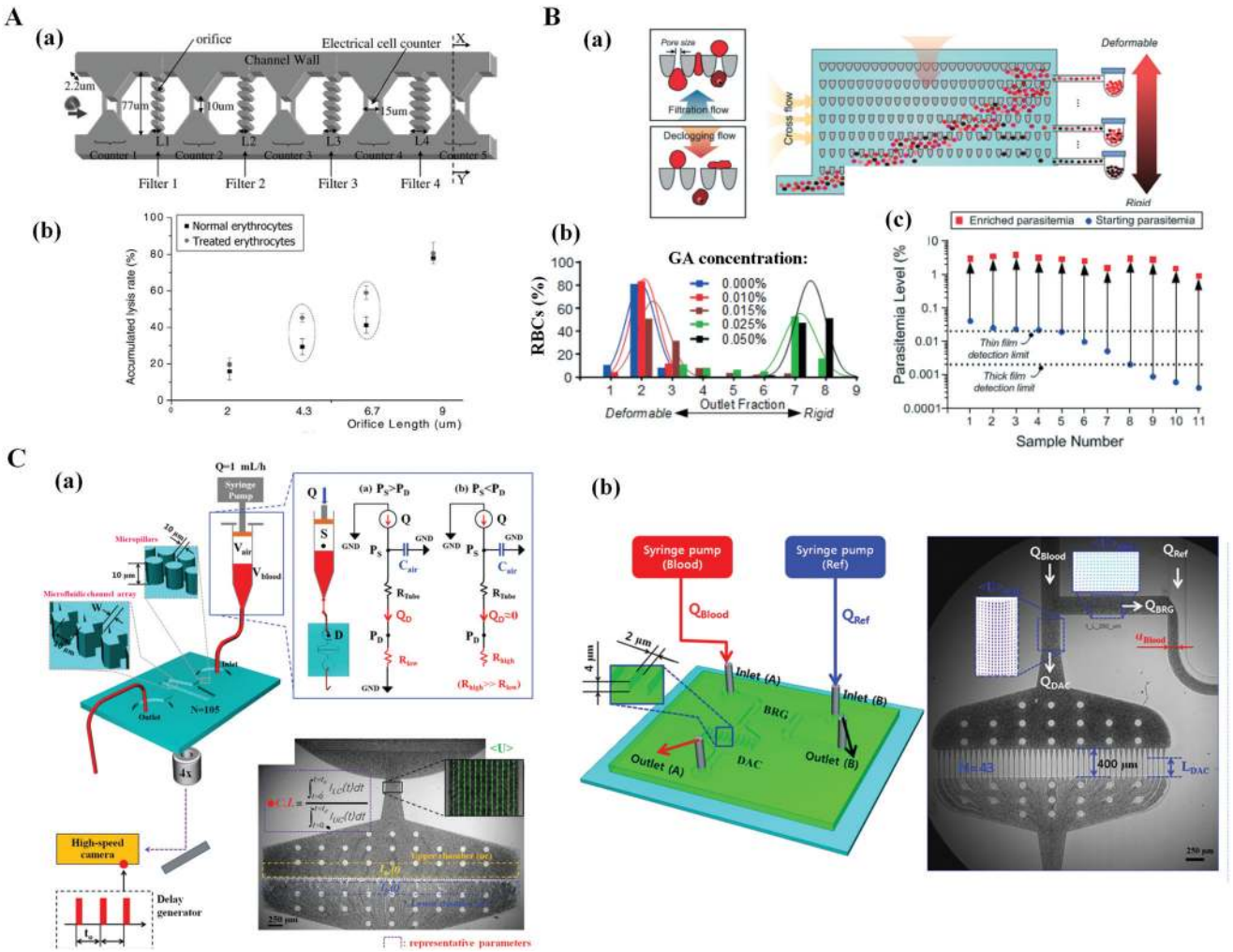

Fig. 6 Microfluidic-based measurement of RBC deformability using strain-dependent cell-lysis rate, deformability-based sorting, and hemodynamic variation. (A) Measurement of strain-dependent cell-lysis rate.[80] (a) Schematic of a microfluidic device. (b) Accumulated lysis rate of normal and chemically-treated RBCs with respect to orifice length. (B) Deformability-based sorting in a ratchet-sorting device.[81] (a) Sorting of cells using a taper funnel constriction. (b) Normalized distribution across the outlets of RBCs treated with various concentrations of GA. (c) Enrichment of malaria-infected RBCs with parasitemia level from 0.0004% to 0.04%. (C) Variations in hemodynamic parameters of blood flows in parallel micro-pillars. (a) Temporal variations in the velocity and image intensity of blood flow in the micro-pillars of a symmetric zigzag shape.[83] (b) Variations in blood velocity in DAC and blood-filled width in a single right-side channel.[65] Reproduced from ref. 65, 80, 81, and 83 with permission from the American Chemical Society, IEEE-Inst Electrical Electronics Engineers Inc., and Royal Society of Chemistry.

fluidic device. The microfluidic device was designed by mimicking a Wheatstone-bridge electric circuit.[62] To measure RBC deformability accurately, the deformability assessment chamber (DAC) installed at the left lower-side channel had parallel micro pillars (N = 43, gap = 2 μm, depth = 4 μm, length = 50–250 μm), as shown in Fig. 6C-(b). After supplying blood (haematocrit = 50%) and 1× PBS solution to each inlet, blood volume as a deformability index was evaluated by integrating the average blood velocity for a certain period. Blood velocity[65] or viscoelasticity[62] was measured by monitoring the blood-filled width in the right lower-side channel. The blood volume was significantly decreased as parasitemia increased. When parasitemia was greater than 0.515% for the ring stage, 0.0544% for the trophozoite stage and 0.0054% for the schizont stage, blood velocity exhibited an unstable behaviour due to the cytoadherence of malaria-infected RBCs to the inner surface of the microchannel.

2.2.4 Optical stretcher-based measurement of RBC deformability. Kaminski *et al.*[84] suggested a microfluidic optical cell stretcher for measuring the elasticity of malaria-infected RBCs. Fig. 7A shows a schematic of the optical stretcher, the operational sequence of the experiment and the deformation behaviours of control and trophozoite stage-infected RBCs. As shown in Fig. 7A-(a), two light-delivering opposing fibers were supported and aligned by a cross-shaped photolithographic pattern on the glass slide. The superposed light created a stable trap. As shown in Fig. 7A-(b), RBCs were trapped and stretched depending on the light intensity. Fig. 7A-(c) and (d) showed typical cell edges in trapped and stretched states. The cell elongation (*i.e.*, the normalized major axis) was then

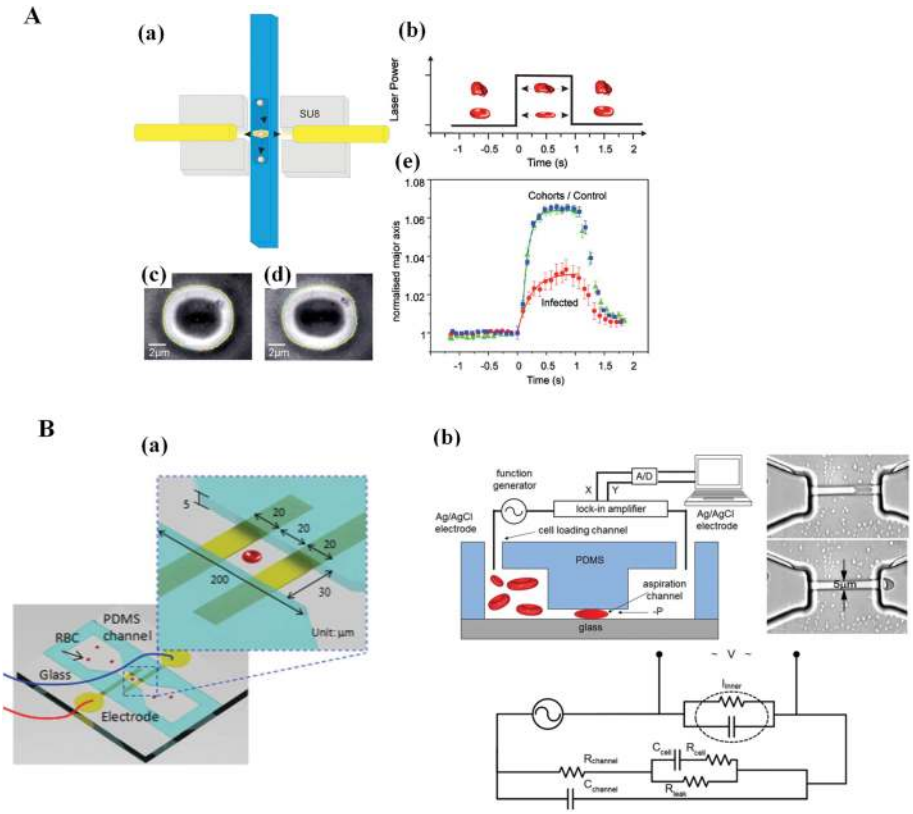

Fig. 7 Microfluidic-based measurement of RBC deformability using optical stretching and electrical impedance. (A) Measurement of cell elongation using an optical stretcher.[84] (a) Schematic of the optical stretcher. (b) Sequence of operation. (c) Normal RBCs trapped at low light intensity. (d) Normal RBCs elongated at high light intensity. (e) Deformation comparison between normal RBCs and malaria-infected RBCs. (B) Variation in electric impedance of individual RBCs flowing in a straight constriction channel. (a) Experiment setup for the measurement of the electrical impedance of single RBCs using a microfluidic channel.[85] (b) Simultaneous measurement of electrical impedance and transit time of individual RBCs in the constriction channel.[86] Reproduced from ref. 84, 85, and 86 with permission from the Royal Society of Chemistry and SPIE-Soc Photo-Optical Instrumentation Engineers.

measured by conducting ellipse fitting on cell edge pixels along the axis of the optical fibers. Fig. 7A-(e) showed temporal variations of the normalized major axis with respect to controls, cohorts, and malaria-infected RBCs. Cohorts (squares, n = 32) and controls (triangles, n = 46) exhibited very similar compliance. But the compliance of malaria-infected RBCs (circle, n = 24) was greatly reduced compared with the control. According to the Kelvin–Voigt model, which assumes that viscosity (μ) and elasticity (E) are connected in series for each cell, the strain [$\varepsilon(t)$] under constant stress (σ) can be described as $\varepsilon(t) = a[1 - \exp(-\lambda t)]$. Here, $\lambda = E{\cdot}\mu^{-1}$ represents the characteristic deformation rate. $a = \sigma{\cdot}E^{-1}$ denotes the relative amplitude of the stretch. Both parameters (a and λ) were obtained by conducting a curve-fitting procedure from cell elongation information measured by using an optical fibre. The values of a and λ in the malaria-infected RBCs decreased by a factor of 2 to 3 compared with those in the normal RBCs. Both parameters (a, λ) were significantly varied due to the existence of malaria parasites in RBCs. Given that the technique was implemented in a non-contact manner, the results were free from artefacts induced by physical contact required in other single-cell measurement techniques.

2.2.5 Electrical impedance-based measurement of RBC deformability. Chandrakasan *et al.*[85] used electric impedance (EI) micro-flow cytometry to characterise the disease state of single cells. The platform provided a label-free and non-invasive cell-counting assay with sensing electric impedance. As shown in Fig. 7B-(a), the microfluidic device was composed of a constriction channel (width = 30 μm and depth = 5 μm) and two electrodes (interspace = 20 μm, width = 20 μm and depth = 0.1 μm). To check the pathological states of individual cells, a dimensionless offset parameter (δ) was obtained by a linear combination of phase and magnitude changes in electric impedance. The experimental result indicated that the proposed method can effectively differentiate malaria-infected RBCs from normal RBCs.

To achieve a high throughput in biophysical measurements of RBCs (*i.e.* 100 cells per 1 s to 150 cells per 1 s), Sun *et al.*[86] used multiple parameters, including mechanical properties (transit time) and electrical signals (impedance amplitude ratio and impedance phase increase). As shown in Fig. 7B-(b), electrical impedance was measured as RBCs flowed through a straight constriction channel (width = 5 μm and depth = 3 μm). The histograms obtained from the multiple parameters

for adult and neonatal RBCs showed distinctively different biophysical properties.

2.2.6 Discussion on RBC deformability measurements. As summarised in Table 2, several measurement techniques, including cell blockage, cell aspiration, cell transit, optical stretcher and electrical impedance, have been developed to measure the deformability of individual RBCs using microfluidic devices. Clinical applications require the detection of a large number of RBCs for high-throughput analysis.[87] In addition, establishing a standard protocol for each measurement is essential because several factors, such as storage time, temperature and osmotic pressure, affect RBC deformability. Among the several techniques used for RBC deformability, the cell transit-based technique might have a strong potential for use in high-throughput screening. By injecting individual RBCs into a microfluidic device with funnels or micropillars, RBC deformability was evaluated at a high throughput (*i.e.* 10^5 RBCs per 200 s) in a previous study.[65] However, because this method utilises a high-speed camera and digital image processing, it presents a technical bottleneck when applied in clinical settings. Thus, instead of the imaging-based analysis technique, the analytical sensor-based technique could be alternatively adopted for clinical applications. It could be employed to effectively monitor pathological changes in blood circulating under *ex vivo* conditions.

2.3 RBC aggregation measurement using microfluidic devices

RBCs suspended in plasma aggregate and form rouleaux at stasis or under low shear rates. The aggregated RBCs are dispersed at high shear rates. Thus, RBC aggregation is significantly varied by (i) intrinsic cellular properties (membrane deformability and surface charge density), (ii) suspending medium properties (fibrinogen concentration in plasma and aggregation-induced macromolecules) and (iii) shear rate of blood flow in RBCs.[88] RBC aggregation has been explained using cross-bridge[89] and depletion-induced[90,91] models. The depletion-mediated model is favoured over the cross-bridge model for understanding the interactions of RBCs.[89] RBC aggregation is considered the determining parameter of haemorheological properties and exerts a direct influence on blood viscosity and microcirculation at low shear rates. Clinically, RBC aggregation is enhanced in various pathological diseases, including malaria, diabetes, hypertension, sepsis and microcirculatory disorders.

To quantify the RBC aggregation of blood samples in a microfluidic platform, blood is supplied to a microfluidic channel. Thereafter, to induce the aggregation or disaggregation of RBCs, blood flow is agitated or stopped by using external devices, such as a syringe pump,[34,92] a vacuum pump,[93,94] a stirring system,[95,96] a vibration system[97] and a pinch valve.[61,88] A typical syllectogram is obtained as a function of time by quantifying blood flows through several methods, including the measurement of photometric intensity (light transmission and light backscattering) and electrical impedance and capturing of microscopic or speckle images. As shown in Fig. 8A-(b), a typical aggregation index (AI) is evaluated with the ratio of the area under the curve (S_A) to the total area of the curve ($S_A + S_B$) [*i.e.*, $AI = S_A/(S_A + S_B)$].[98] This section focuses on several measurement techniques for characterising RBC aggregation using microfluidic platforms. The techniques are summarized in Table 3.

2.3.1 Photometric intensity-based measurement of RBC aggregation. Shin *et al.*[93,94] proposed a microfluidic aggregometer for measuring RBC aggregation in a microfluidic channel. As shown in Fig. 8A-(a), the aggregometer was composed of a microfluidic device (width = 4 mm, depth = 200 μm and length = 40 mm), a laser as a light source, a photodiode for measuring light reflection, a pressure sensor and a vacuum pump. After dropping 0.5 mL of a blood sample into a sample chamber, the microfluidic channel was filled with blood by operating the vacuum pump. The RBCs were aggregated or dispersed depending on the flow rate. By measuring the light intensity reflected from the blood sample with a photodiode, the RBC aggregation index was calculated by analysing temporal variations in backscattered light intensity. Fibrinogen in plasma was found to increase RBC aggregation. It also increased critical shear stress by about 46% compared with RBCs suspended in PBS solution. The proposed method was applied to examine the effect of temperature on RBC aggregation.[94] Threshold shear stress was introduced to monitor the effect of temperature on the RBC aggregation because the RBC aggregation index did not fully reflect the trends of RBC aggregation with respect to temperature. The threshold shear stress and blood viscosity exhibited similar trends with respect to fluid temperature. Furthermore, the microfluidic device was used to compare the performance of light-transmission and back-scattering methods.[95] Although both methods had a good relationship, they produced different values of the RBC aggregation index. However, when an orthogonal polarization technique was applied, both methods resulted in the same RBC aggregation index for various blood samples mixed with different concentrations of dextran solution.

ESR is a simple clinical index for screening several inflammatory diseases. To investigate the relationship between RBC aggregation and ESR, Elbuken *et al.*[88] developed a microfluidic opto-electro-mechanical system.[88] As shown in Fig. 8A-(b), the microfluidic system was composed of a solenoid pinch valve for disaggregating RBCs in whole blood, a photodetector for detecting light intensity transmitted from a light-emitting diode (LED), a microfluidic cartridge and an optical microscope equipped with a camera. The microfluidic cartridge had a deep channel (width = 1 mm and depth = 1 mm) for ESR and a shallow channel (width = 44.5 mm and depth = 150 μm) for RBC aggregation. A solenoid pinch valve was employed to provide back-and-forth blood flow continuously in the cartridge for 15 s. The principle of this measurement system was based on the analysis of optical light transmitted through blood samples. An infrared light-emitted diode (LED) of 830 nm in wavelength was placed at the top surface of the cartridge, and illuminated the blood-filled channel. The light

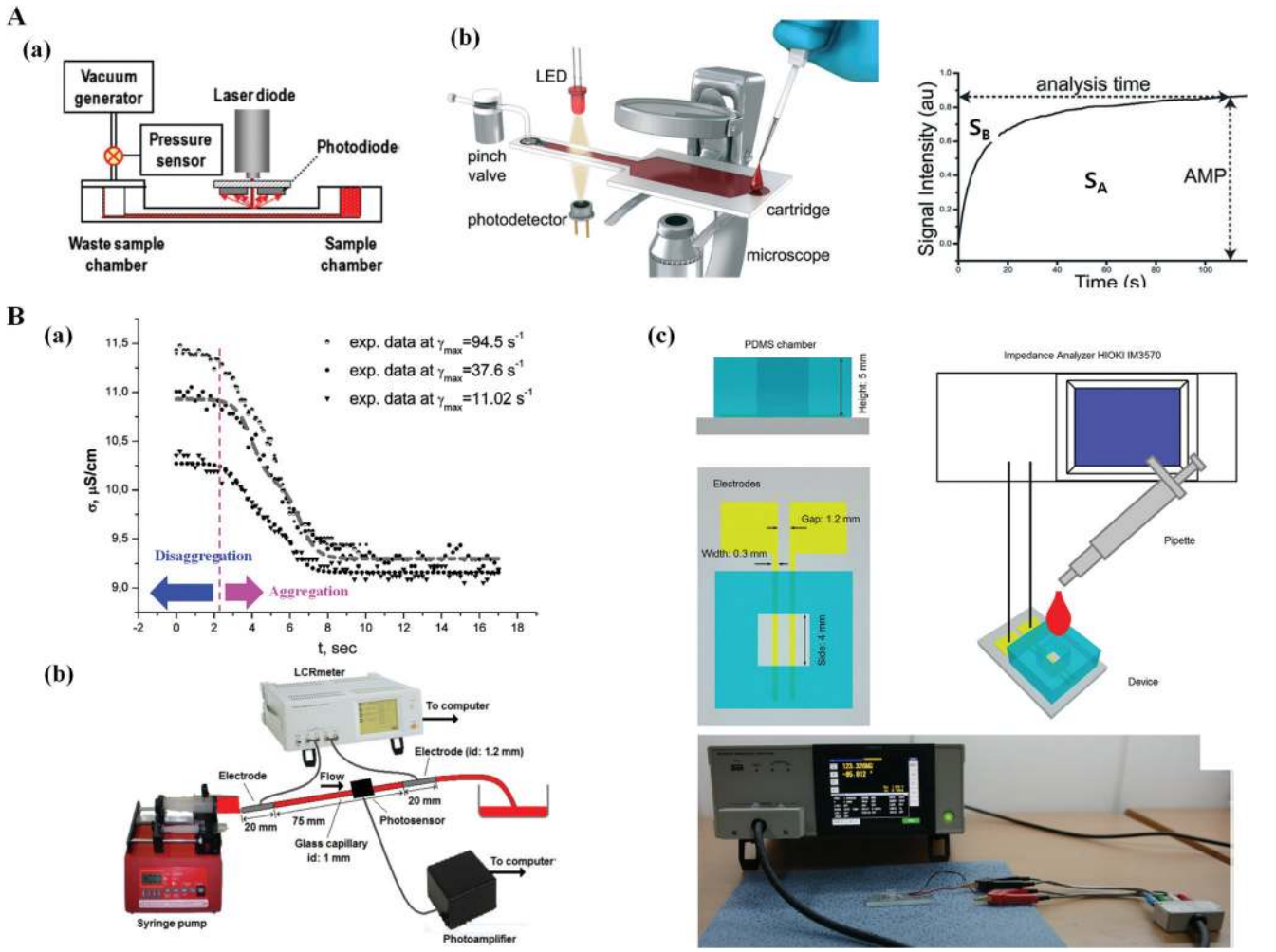

Fig. 8 Microfluidic-based measurement of RBC aggregation by analysing photometric intensity and blood conductivity. (A) RBC aggregation measurement from the photometric intensity. (a) Microfluidic aggregometer including a vacuum pump, a pressure sensor, a microfluidic channel and a laser-photodetector.[94] (b) The microfluidic system used for the measurement of the erythrocyte sedimentation rate (ESR) and erythrocyte aggregation.[88] (B) The measurement system used for blood conductivity. (a) Variations of blood conductivity with respect to shear rate during aggregation.[99] (b) Schematics of the electrical impedance measurement system.[98] (c) A microfluidic device with a gold-plated electrode and an impedance analyser.[101] Reproduced from ref. 88, 94, 98, 99, and 101 with permission from the Royal Society of Chemistry, Public Library Science, IOS Press, Elsevier Sci. Ltd, and IEEE – Institute of Electrical and Electronics Engineers.

passing through the channel was collected on the photodetector located at the bottom of the cartridge. After supplying the blood sample into the cartridge, the test was started by fully disaggregating RBCs for 15 s with the aid of a pinch valve. By turning off the pinch valve, RBCs were aggregated immediately. During the aggregation process, the blood sample was illuminated with the LED. Using a photodetector, the transmitted light intensity was consecutively recorded for 120 s. It was employed to calculate the aggregation index. Linear regression analysis showed that the conventional RBC aggregation index did not provide significant relationship information on conventional Westergren ESR. To obtain a sufficient relationship between microfluidic ESR and Westergren ESR, a microfluidic ESR index was proposed to examine amplitude variations in light intensity (ΔI) at an elapsed time of t = 120 s [*i.e.*, $\Delta I = I(t = 120\ \text{s}) - I(t = 0)$]. $I(t$ = 120 s) and $I(t = 0)$ denote the light intensity at t = 120 s and t = 0, respectively. The proposed method quantified RBC aggregation by analysing the transmitted light intensity obtained from the shallow channel of the microfluidic cartridge.

2.3.2 Electrical conductivity-based measurement of RBC aggregation. Temporal variations in blood conductivity can be used to estimate RBC aggregation. Antonova *et al.*[99] presented a Couette viscometric system composed of a rotational viscometer and a conductivity measurement device. Given that the electrical properties of blood in a simple shear flow were varied depending on the frequency and shear rate,[100] conductivity signals of 2 kHz were recorded under the condition of a transient shear rate ranging from 0.94 s^{-1} to 94.5 s^{-1}. Blood conductivity varied depending on several factors, including the shear rate, haematocrit, and temperature. As shown in Fig. 8B-(a), during RBC aggregation, blood conductivity was largely

Table 3 Summary of microfluidic-based techniques for measuring RBC aggregation

Principle	Measurement quantity	Test cell	Comment	Ref.
Photometric method (transmission, scattering)	Light intensity and shear stress	RBC in fibrinogen suspension	Scattered light (laser, photodiode)	93 and 94
	Light transmission or back scattering		Blood delivery with a vacuum pump	
	Light intensity and microscopic image	RBC in dextran suspension	RBC disaggregation with a pinch valve Comparison of ESR and RBC aggregation	88
Electrical conductivity	Conductivity	RBC in plasma	Comparison of ESR and conductivity	99 and 101
Microscopic image	Aggregation size Velocity field Cell-depleted layer	Whole blood (haematocrit = 25%)	Image processing Partitioning of RBC aggregation in a T-shaped bifurcation channel	102 and 103
	Speckle size	RBC in dextran suspension Diabetic rat blood	Single channel Comparison of ultrasonic, microscopic image and ESR	104
	Cluster size and occurrence	RBC in dextran or fibrinogen suspension	*In vivo* or *in-vitro*	105
	Image intensity	Malaria-infected blood (haematocrit = 30%)	ESR measurement with a syringe pump	92
		RBC in dextran suspension		
		RBC in dextran suspension	Periodic on-off control of blood flow Simultaneous measurement	34
		RBC in dextran suspension	Periodic delivery with a disposable pump RBC aggregation under continuous sedimentation	61

decreased depending on the shear rate. In addition, the system can provide valuable information on rouleaux formation or structural transformation of RBC aggregates during the aggregation–disaggregation process.

Meiselman *et al.*[98] compared RBC aggregations by analysing the transmitted light intensity and electrical impedance signals as shown in Fig. 8B-(b). Electrical impedance of 100 kHz and light transmittance were recorded under a high shear flow and for 120 s after abrupt stoppage of blood flow, during which RBC aggregation occurs. RBC aggregation was then quantified from capacitance values obtained from electrical impedance data. The RBC aggregation parameters derived from capacitance data were in good agreement with those obtained from light transmittance data.

Yang *et al.*[101] established a microfluidic-based ESR measurement method by monitoring temporal variations in electrical impedance signals of blood with various haematocrits. As shown in Fig. 8B-(c), the microfluidic-based conductivity measurement system was composed of a PDMS chamber with a square cross section (width = 5 mm and depth = 5 mm) and two gold-deposited planar electrodes (thickness = 0.3 μm and width = 300 μm) that were 1200 μm apart. After a blood sample was dropped into the PDMS chamber, the electric conductivity of the test blood was measured with an impedance analyser. The measured blood conductivity increased for the first 1 min and decreased thereafter. Theoretical analysis revealed that the initial increase in blood conductivity was caused by RBC aggregation, and the subsequent decrease resulted from the deposition of RBCs. The ESR value obtained from the electrical impedance signal showed a sufficient correlation with the standard Westergren ESR method.

2.3.3 Microscopic image-based measurement of RBC aggregation. Local RBC aggregation in micro-scale blood flows or bifurcating microchannel flows is important because the blood flow and haematocrit are not uniform. For this reason, Balabani *et al.*[102,103] investigated spatial distributions of RBC aggregation in a T-shaped bifurcation. Fig. 9A shows a schematic of the microfluidic system. A pressure control device was employed to supply blood from the parent conduit (P) (width = 100 μm and depth = 40 μm) towards two daughter branches (L and R). The velocity field and streamlines of RBC aggregation at a flow rate of $Q_D/Q_P = 0.13$ are shown in the right panel of the figure. Q_P and Q_D denote the flow rate of the parent and right daughter conduits, respectively. The size of RBC aggregation was determined by adopting an image processing technique. The mean aggregated size was marginally increased in the daughter branches mainly due to low shear rates. This result was attributed to the depletion of RBC aggregation in certain regions of the parent conduit and to the change in the flow-split location in the T-junction with respect to the flow rate ratio.

Lee *et al.*[104] conducted a microfluidic-based speckle analysis for the sensitive measurement of RBC aggregation. As shown in Fig. 9B, the microfluidic device had a single inlet, a straight channel (width = 1 mm, depth = 50 μm and length = 10 mm) and a single outlet. After selecting a specific region of interest (ROI) of 128 × 128 pixels, the normalized autocorrelation function (f_{auto}) was calculated along the horizontal and vertical directions. The size of the speckle pattern (S_H and S_V) was estimated as the corresponding width at half of f_{auto} (f_{auto} = 0.5). Then, the average speckle area ($A_{Speckle}$) was evaluated by multiplying the horizontal and vertical speckles (*i.e.* $A_{Speckle} = S_H \cdot S_V$). As shown in the right figures, the speckle patterns

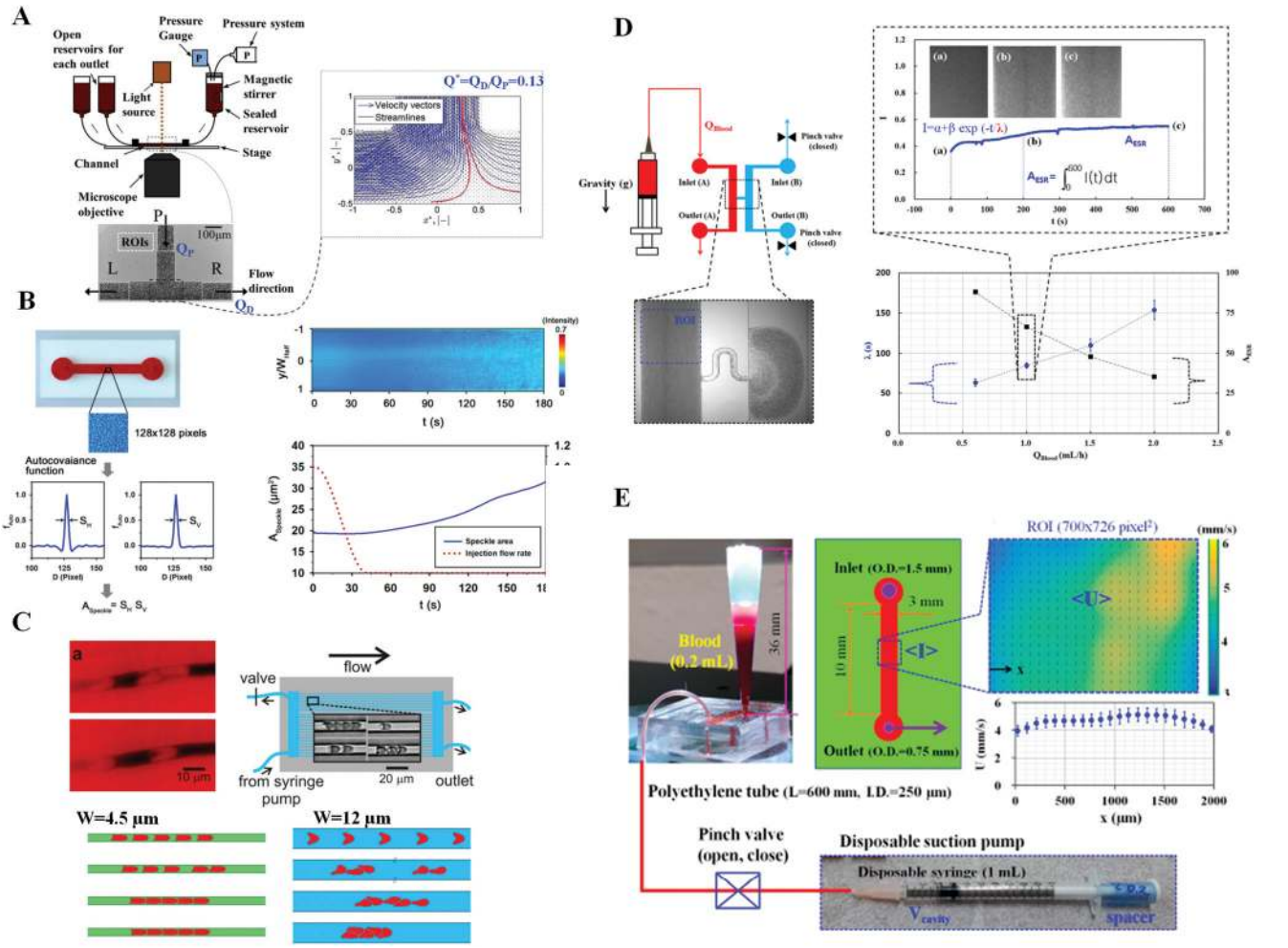

Fig. 9 Microfluidic-based measurement of RBC aggregation by analysing microscopic images of aggregated RBCs in a microfluidic channel. (A) Spatial distributions of RBC aggregations in T-shaped bifurcation.[102] (B) Analysis of speckle patterns in a straight microfluidic channel.[104] (C) Cluster size and occurrence of RBCs in micro-capillary flows.[105] (D) Microfluidic-based ESR measurement using a disposable syringe by analysing the image intensity of blood flow in a microfluidic channel.[92] (E) Variation in RBC aggregation owing to continuous ESR in a conical pipette tip under periodic on–off blood delivery by using a disposable suction pump.[61] Reproduced from ref. 61, 92, 102, 104, and 105 with permission from MDPI AG, AIP Publishing, and Nature Publishing Group.

appeared over time. After the flow of blood (RBC suspended in 0.06% dextran solution, haematocrit = 40%) was stopped, $A_{Speckle}$ gradually increased. Through quantitative comparisons with conventional measurement methods, including the conventional ESR method, microscopic observation and ultrasound imaging, the speckle area ($A_{Speckle}$) can be used to evaluate RBC aggregation effectively.

Wagner *et al.*[105] investigated the effects of dextran and fibrinogen on RBC aggregation in micro-capillaries. Fig. 9C shows a cluster of RBCs passing through a capillary vessel of a mouse, a microfluidic device (N = 30, width = 8.5 μm and depth = 4.5 μm) and the numerical simulation result on the effect of fibrinogen on two different channel widths (w) (w = 4.5 and 12 μm). At high shear rates in the micro-capillaries or low haematocrit of 1%, fibrinogen or dextran enhanced the formation of robust clusters of RBCs. This persistent RBC aggregation exerted an influence on the spatial distribution of RBCs and blood perfusions in microvascular networks.

Lee *et al.*[92] reported a microfluidic-based ESR measurement technique to detect malaria-infected RBCs collected from a mouse. As shown in Fig. 9D, a disposable syringe filled with blood was turned upside down in the gravitational direction. When blood was supplied to a microfluidic device from the top of the syringe, the haematocrit of the blood decreased due to continuous ESR in the syringe. By assuming the image intensity of blood flow as $I(t) = \alpha + \beta \exp(-t/\lambda_{ESR})$, the dynamic variation in ESR was evaluated with two parameters, namely, the time constant (λ_{ESR}) and ESR area (A_{ESR}). The two parameters varied significantly when RBCs were suspended in a dextran solution (haematocrit = 30%). The ESR and viscosity of malaria-infected RBCs increased significantly with respect to the parasitemia level.

Kang[61] proposed a microfluidic-based technique for measuring RBC aggregation under haematocrit variation due to continuous ESR in the tip of a conical pipette. As shown in Fig. 9E, a conical pipette tip was tightly fitted into the inlet

port, and a disposable suction pump was connected to the outlet. After dropping blood (~0.2 mL) into the conical pipette tip, blood flow was turned on and off by periodically operating a pinch valve. To effectively evaluate variations in RBC aggregation due to continuous ESR, an erythrocyte sedimentation rate aggregation index (EAI) was newly defined from temporal variations in the image intensity of blood flows in the microfluidic channel. EAI was more effective than the conventional AI in monitoring variations in RBC aggregation due to continuous ESR. In addition, the EAI gradually increased with the increase in the concentration of the dextran solution.

Kang[34] suggested a simple method for the continuous and simultaneous measurement of biophysical properties of blood, including viscosity, viscoelasticity and RBC aggregation. The blood sample was precisely delivered into the inlet (A) under pulsatile flow rate conditions. However, PBS solution was supplied to the inlet (B) at a constant flow rate. By operating a pinch valve connected to the outlet (A), blood flow was stopped or allowed to pass through the lower left channel. Then, the biophysical properties of blood were quantified by analysing the flow rate in the upper left channel ($Q_{\mu PIV}$), image intensity in the lower left channel ($\langle I\rangle_{Blood}$) and blood-filled width in the lower right channel (α_{Blood}). To consistently measure RBC aggregation, the value of $\langle I\rangle_{Blood}$ was obtained from the corresponding time of the minimal image intensity ($\langle I\rangle_0$) for 100 s. RBC aggregation was then evaluated in terms of the linear slope of the image intensity ($\langle I\rangle_{slope}$), the integral of the image intensity above the minimal image intensity for 100 s (A_{upp}), the integral of the minimal image intensity for 100 s (A_{low}), and the ratio of A_{upp} to A_{low} (*i.e.*, $A_{ratio} = A_{upp}/A_{low}$). Three parameters ($\langle I\rangle_{slope}$, A_{ratio} and A_{upp}) defined from $\langle I\rangle_{Blood}$ were varied significantly depending on RBC aggregation. The addition of dextran solution increased blood viscosity and RBC aggregation. However, a glutaraldehyde solution did not contribute to varying RBC aggregation.

2.3.4 Discussion on RBC aggregation measurement techniques. As summarised in Table 3, several RBC aggregation measurement techniques, including photometric intensity, electric conductivity, and microscopic images, have been used to quantify RBC aggregation flowing in a microfluidic device. By agitating RBCs with a disaggregation mechanism, RBC aggregation was quantified by analysing light intensity, electric conductivity and image intensity. Compared with measurements of blood viscosity and RBC deformability, RBC aggregation has been widely adopted to detect various pathological diseases in clinical settings. Using a microfluidic platform, the effects of plasma protein (*i.e.* fibrinogen) or dextran solution on RBC aggregation were examined by monitoring the size of clusters or the cell-depleted layer of RBCs in microfluidic channels or capillary networks.[102,105] In addition, RBC aggregation and ESR were simultaneously measured by analysing light transmission intensity and microscopic images.[88] Recently, a new RBC aggregation index (EAI) was proposed to monitor variations in RBC aggregation due to continuous ESR in reservoirs.[61] However, because all methods were developed to measure RBC aggregation under *in vitro* conditions, several issues (blood collection, storage time, and hemodilution) hinder measuring the RBC aggregation of real blood circulating in a closed *ex vivo* circuit. Thus, improving or modifying these methods is required for the measurement of RBC aggregation under *ex vivo* conditions.

3. *Ex vivo* blood physical analysis of an animal model

To quantify various biophysical properties of blood circulating in complex fluidic circuits, including hemodialysis[106] and a cardiopulmonary-bypass procedure,[107,108] blood samples have been collected from conduits. Then, the haemorheological properties of the blood were measured under *in vitro* conditions.

Whittaker *et al.*[109] reported that blood viscosity measured with an Oswald viscometer (*in vitro* conditions) is higher than that estimated based on the pressure and flow rate curve for the hind limb of a dog (*in vivo* conditions). This result is attributed to the much larger diameter of the Oswald viscometer (inner diameter = 930 μm) compared with that of real blood vessels. The Fahraeus–Lindqvist effect,[110] which depends on vessel diameter owing to the cell-free layer,[111,112] endothelial glycocalyx[113] and vasomotor control,[114] contributes to the difference in blood viscosities measured by *in vivo* and *in vitro* experiments.[43] Given the different geometries between blood vessels and *in vitro* instruments, *in vitro* methodology cannot provide consistent rheological properties of blood compared with *in vivo* measurement techniques, including electrical impedance catheters,[115,116] photo-acoustic and photo-thermal cytometry,[117] cellular ultrasound imaging method[118] and microscopic image-based velocimetry.[119,120] In addition, haemorheological properties are significantly varied due to the presence of artefact (blood–air interface)[121] and storage conditions.[122,123] During blood collection, haemodynamic properties, including flow rates or pressures in the closed conduit, are not specified. For this reason, haemorheological properties of blood have been measured over a wide range of shear rates, rather than at a specific shear rate condition. Considering that blood collections decrease the blood volume in the closed loop, a lactated Ringer's solution is applied to maintain blood volume during cardiopulmonary bypass procedures.[107] However, this hemodilution causes to vary the haemorheological properties significantly. To minimise or remove blood collection from the closed conduit, various methods have been suggested to quantify the biophysical properties of real blood circulating under *ex vivo* conditions.[124,125] The measurements of haemorheological properties under *in vivo* and *ex vivo* conditions are summarized in Table 4.

3.1 Microfluidic-based haemorheological measurements under *ex vivo* conditions

Lee *et al.*[42–44,126–128] used an extracorporeal rat bypass loop to study microvascular haemodynamics. As shown in Fig. 10A-(a),

Table 4 Summary of haemorheological property measurement under *in vivo* and *ex vivo* conditions

Experimental condition	Measurement quantity	Animal model	Comment	Ref.
In vivo	RBC velocity	Venule (rat)	Effect of RBC aggregation on velocity profile in venule	120
	Blood viscosity	Right atrium (10 patients) On-pump heart surgery	Electrical impedance technique with central venous catheter	115 and 116
	Blood velocity Haematocrit RBC aggregation Blood viscosity	Nude mouse	Photo-acoustic and photo-thermal flow cytometry	117
	RBC aggregation Flow rate	Diabetic patients	Ultrasound imaging (aggregation size)	118
	Blood velocity Wall shear stress	LPS-stimulated zebrafish	Discrete circuit model	119
Ex vivo	Velocity profile Pulsatility index	Rat	Micro-PIV technique Three pinch valves for controlling blood flow	126
	Blood viscosity Flow rate Pressure	Rat	Microfluidic device Discrete circuit model Periodic blood collection (required)	42 and 43
	Blood viscosity Pressure RBC aggregation Velocity profile	Rat	Hybrid system (microfluidic device and ultrasound system) Discrete circuit model Periodic blood collection (required)	44
	Image intensity Pressure drop Clotting time	Pig	Shear gradient microfluidic device Monitoring whole blood hemostasis and platelet function	125

an extracorporeal rat bypass loop was constructed by connecting a fluorinated ethylene propylene (FEP) tube from the jugular vein to the femoral artery. Microscopic images of blood circulating in the loop were sequentially captured with a high-speed camera. The velocity profiles of blood flow in the bypass FEP tube were obtained by conducting the time-resolved micro-particle image velocimetry technique for microscopic images of blood flows. As shown in Fig. 10A-(b), the centre velocity in the bypass FEP tube can be controlled by adjusting the main tube with a pinch valve. The ratio of the systolic blood velocity to the diastolic blood velocity decreased with increasing blood flow rate. The blood rate and amplitudes of pulsatile blood flow can be easily controlled by adjusting the pinch valves installed in the arteriovenous shunt loop. Therefore, the proposed bypass loop had a strong potential for obtaining haemodynamic information on real blood flows.

Given that previous *in vitro* experiments measured blood viscosity under a specific flow rate, their methods are lacking when used to evaluate blood viscosity at unspecified flow rates. For this reason, a flow rate sensor is installed in the closed fluidic circuit to measure the blood flow rate. However, tedious cleaning or calibration is required after each experimental measurement. To resolve this problem, a twin-shaped microfluidic device was introduced in a previous study for the simultaneous measurement of viscosity and flow rate of whole blood circulating in a complex fluidic circuit that includes a rat, a reservoir, a pinch valve and a peristaltic pump.[42] As shown in Fig. 10B-(a), rat blood was delivered to the blood reservoir at an unknown flow rate (Q_x) by adjusting the pinch valve. The blood was supplied to the microfluidic device using a peristaltic pump at a specific flow rate. The microfluidic device was composed of two half-circular chambers (diameter = 22 mm and depth = 50 μm), two side channels with multiple microchannels (N = 25, width = 300 μm and depth = 50 μm) connected by a bridge channel. Firstly, by using reversal flow switching manipulation in the bridge channel,[15] blood viscosity was measured under two different blood flow rate conditions [(a) specified flow rate *via* a syringe pump and (b) unspecified flow-rate *via* a peristaltic pump]. The blood flow rate (Q_{Blood}) and blood viscosity (μ_{Blood}) were simultaneously measured with good measurement accuracy and reliability. Then, the viscosity of rat blood flowing in the complex fluidic network was measured. The number of channels filled with blood (N_{Blood}) remained constant at N_{Blood} = 18–19, as shown in Fig. 10B-(b), due to the compliance effect of the half-circular chamber. By using two distinctive relationships (N_{Blood} *vs.* Q_{Blood}, μ_{Blood} *vs.* Q_{Blood}) that were experimentally obtained, the viscosity of rat blood was evaluated as 5.89 ± 0.08 cP at a flow rate of 3.8 mL h^{-1}. Through experimental demonstrations, the proposed method was found to be a promising technique for effectively evaluating the flow rate and viscosity of whole blood circulating in a complex fluid network without sensors and tedious labelling procedures. In addition, it will be employed to measure temporal variations of blood viscosity during a cardiopulmonary bypass procedure or haemodialysis.

To monitor temporal variations in the biophysical properties of rat blood, including viscosity, flow rate and pressure,

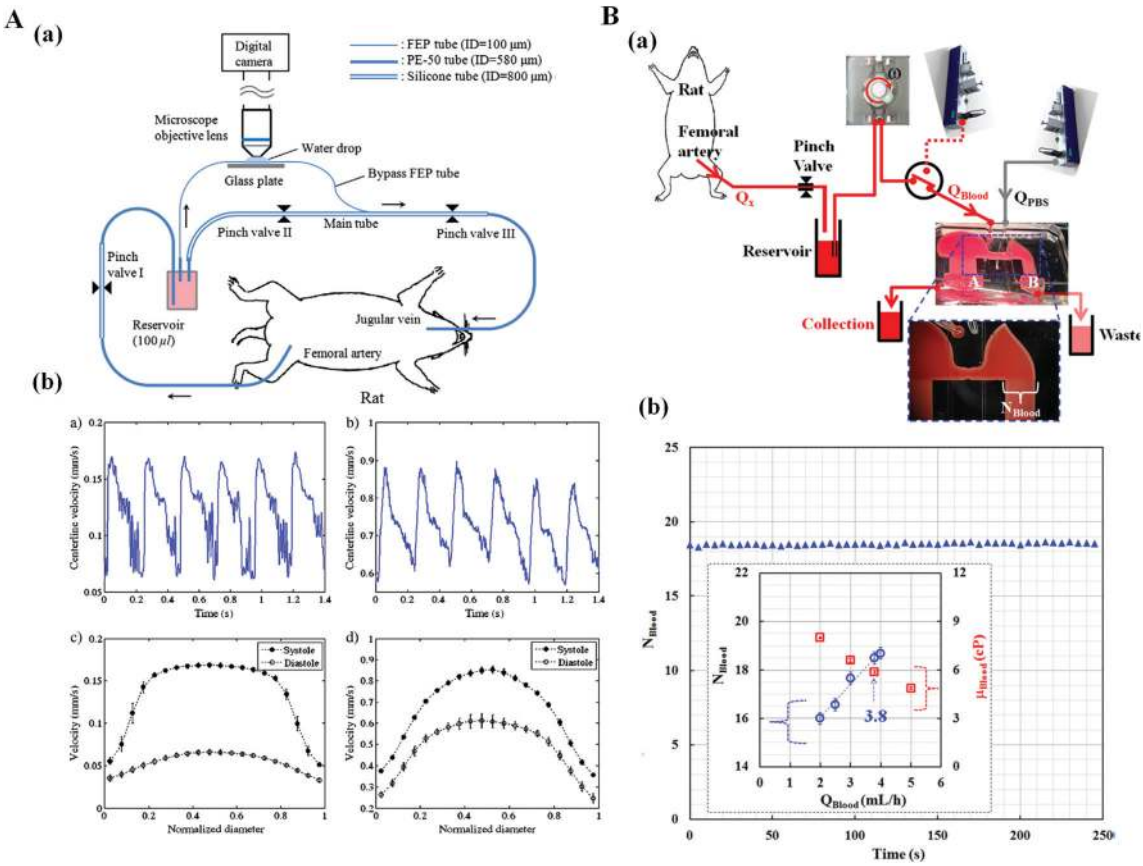

Fig. 10 Microfluidic-based measurements of haemorheological properties under *ex vivo* conditions. (A) Extracorporeal rat bypass loop for hemodynamic analysis.[126] (a) Schematic of an experimental setup including an extracorporeal bypass fluidic conduit, three pinch valves and a microscopic image acquisition system. (b) Variations in centreline velocity and velocity profiles at systolic and diastolic phases. (B) Simultaneous measurement of viscosity and flow rate of blood flow in a complex fluidic circuit.[42] (a) Schematic of an experimental setup including a rat, a pinch valve, a reservoir, a microfluidic device, a peristaltic pump and a syringe pump. (b) Temporal variation in the number of indicating channels filled with blood in the right-side channel. The inset shows two distinctive relationships (*i.e.* N_{Blood} *vs.* Q_{Blood} and w_{Blood} *vs.* Q_{Blood}). Reproduced from ref. 42 and 126 with permission from Academic Press Inc. and American Institute of Physics.

a complex fluidic circuit was established in a study by connecting the abdominal aorta and jugular vein to an extracorporeal bypass loop that includes a flow stabilizer[59,60] and a Wheatstone-bridge analogue microfluidic channel.[15] Based on two consecutive controls for reversal flow switching in the bridge channel,[15] blood viscosity and flow rate were simultaneously measured at a specific duration of time. In addition, the pressure at the abdominal aorta was analytically estimated using a discrete fluidic circuit model. As shown in Fig. 11A-(a), the proposed method was employed to monitor temporal variations in the biophysical properties of rat blood circulating in the fluidic network, especially under a continuous hemodilution condition. After 30 min elapsed, PBS solution was supplied to the inlet (B) at a flow rate of 3 mL h^{-1}. To monitor reversal flow switching in the bridge channel,[15] rat blood of 1 mL h^{-1} was repeatedly collected at intervals of 20 min from the outlet (B) after the stoppage of the syringe pump for the PBS solution. Given that the supplied volume of PBS solution for 20 min (ΔV_{PBS} = 1 mL) was equal to the collected rat blood (ΔV_{Blood} = 1 mL), the overall volume of rat blood was maintained at a constant level under a continuous hemodilution condition (*i.e.* ΔV_{Blood} = ΔV_{PBS} = 1 mL for 20 min). Haematocrit [Fig. 11A-(b)], balancing pressure [Fig. 11A-(c)] and flow rate [Fig. 11A-(d)] gradually decreased due to the continuous hemodilution. The balancing pressure at the left junction (P_X) in the microfluidic channel was estimated using a discrete fluidic-circuit model. As shown in Fig. 11A-(c), the balancing pressure was decreased gradually with the elapse of time. In addition, the blood pressure in the abdominal aorta (P_{rat}) was decreased due to a continuous hemodilution effect. The reduced flow rate contributed to increased blood viscosity [Fig. 11A-(e)]. The proposed method was applied to monitor variations in biophysical properties and platelet aggregation depending on the diabetic duration after streptozotocin treatment in a rat.[127] After collecting blood from the *ex vivo* bypass loop, RBC aggregation was quantified through a modified ESR method.[92,104] The haemorheological properties of the diabetic rat blood were significantly changed compared with those in a normal rat. Platelet adhesion was considerably increased with the increase in diabetic duration. In addition, the proposed

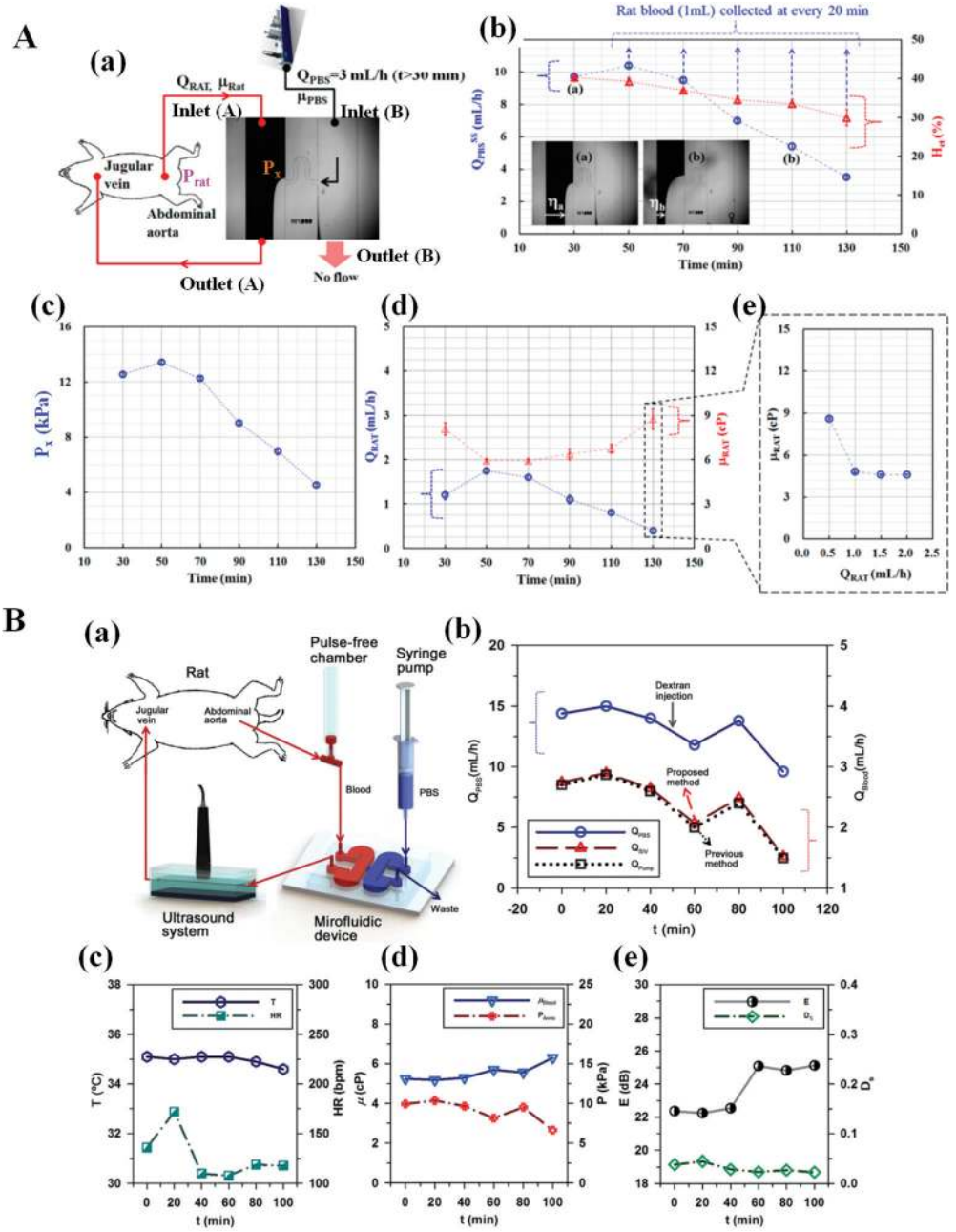

Fig. 11 Microfluidic-based measurements of haemorheological properties under *ex vivo* conditions. (A) Temporal variations in the biophysical properties (viscosity, flow rate and pressure) of rat blood circulating through a complex fluidic network under continuous hemodilution.[43] (a) Schematic of the experimental setup. (b) Temporal variations in switching flow rate of PBS (Q^s_{PBS}) and haematocrit of blood (Hct). (c) Temporal variations in blood pressure at the abdominal aorta (P). (d) Temporal variations in flow rate (Q_{Rat}) and blood viscosity (μ_{Rat}). (e) Variations in blood viscosity with respect to flow rate at a specific time of t = 130 min. (B) Hybrid system used for haemorheological and hemodynamic analysis composed of a microfluidic platform and an ultrasonic imaging system.[44] (a) Schematic of the experimental setup. (b) Temporal variations in switching flow rate (Q^s_{PBS}) and blood flow rate (Q_{Blood}). (c) Temporal variations in temperature (T) and heart rate (HR). (d) Temporal variations in blood viscosity (μ) and pressure at the abdominal aorta (P). (e) Temporal variations in echogenicity (E) and decorrelation (D_s). Reproduced from ref. 43 and 44 with permission from the American Chemical Society and Nature Publishing Group.

method was successfully employed to monitor variations in the biophysical properties of a sepsis rat model established by injection of lipopolysaccharide.[128]

An ultrasound imaging system was additionally employed to monitor RBC aggregation in a rat bypass loop because high shear rates in the microfluidic channel hinder the quantification of RBC aggregation occurring at stasis.[44] As shown in Fig. 11B-(a), the extracorporeal ray bypass loop was constructed by connecting a rat, a pulse-free chamber (or fluidic stabilizer[59,60]), a twin-shaped microfluidic device,[15] a syringe pump

and an ultrasonic imaging system. The biophysical properties of rat blood were measured at intervals of 20 min for 100 min. As shown in the experimental results [Fig. 11B-(b)–(e)], after injecting a specific concentration of dextran solution at 50 min, the echogenicity (E) measured by the ultrasonic system and the blood viscosity (μ) measured by the microfluidic device increased over time due to the enhanced RBC aggregation by the dextran solution. In addition, the mean pressure at the abdominal aorta and flow rate gradually decreased. Experimental demonstration showed that the hybrid system can be effectively used to measure temporal variations in biophysical properties, including RBC aggregation, viscosity, flow rate and blood pressure.

3.2 Blood clotting and cell activation

Under *ex vivo* circulation, a polyethylene tube was used to connect the microfluidic device with blood vessels. The inner surfaces of tubes and microfluidic channels are made to come into direct contact with blood cells. Blood cells adhered on the inner surface of the tubes or microfluidic channels because blood cells are in contact with the non-physiological surface, and this phenomenon could cause interruption in blood flows. When platelets were exposed to high shear stress, they adhered and aggregated to the surface, which hindered blood flows.[127]

The hydrophobic surface properties of silicon-based materials can induce adsorption of plasma proteins, and activate blood clotting sequentially.[129] Due to blood clotting in microfluidic channels or tubes, the functionality of the microfluidic device decreased over time.[59,130,131] By modifying the surface properties of silicone-based materials with PMC polymers, unfavourable protein adsorptions were significantly reduced, compared with uncoated surfaces.[129,132] Since it is difficult to recreate the endothelium in microfluidic channels, a nitric oxide donor or soluble thrombomodulin was added to replace the endothelium.[133] The non-physiological contact surface could be reduced or eliminated by adopting elastomeric blood vessels[134,135] or implanted microfluidic devices.[136,137]

High shear stress and direct contact with sub-endothelial collagen also contribute to activating platelets, and formulating thrombus in microfluidic channels.[130,138] When platelets exposed to high shear stress for a short time were irreversibly activated and aggregated at high shear stress, blood flow was stopped in a microfluidic channel. Thus, platelet aggregation was measured by monitoring the migration distance until the blood flow was completely stopped.[138] Platelet aggregation usually causes to decrease blood flow until it reaches occlusion time. The unstable thrombus detachment increased blood flow suddenly.[131] When blood viscosity was measured by monitoring the interfacial line between two co-flowing streams, platelets were activated and stacked in the interfacial line or surface of the channel. Thus, blood viscosity was inaccurately measured, and continuously varied over time.[59,130]

Several microfluidic devices were introduced to measure coagulation or clotting of blood. Ingber *et al.*[125] suggested a shear gradient-activated microfluidic device for automatic monitoring of platelet function and thrombus formation. Using a microfluidic device mimicked from a network of stenosed arteriolar vessels, blood clotting was evaluated with a small volume of blood under pathophysiological flow conditions. By analyzing clotting time with a mathematical model of thrombus formation, the coagulation and platelet functions could be accurately evaluated through *in vitro* and *ex vivo* experiments. Maddala *et al.*[139] suggested a multi-bypass microfluidics ladder network mimicked from venules to study platelet aggregation and fibrin formation under blood flows. Dynamic blood flow was used to predict the patterns of blood clotting at specific locations in the device. This method provided a correlation between microvascular geometry and thrombus formation under blood flow. Lee *et al.*[130] suggested a correlation mapping for estimating platelet adhesion in a microfluidic channel. The platelet adhesion was evaluated by integrating the area of adhered platelets (A_{platelet}) for a specific time. Under *ex vivo* conditions, they measured platelet adhesion and blood viscosity simultaneously over time. Through a comparative study, the blood viscosity and platelet adhesion of diabetic rats were found to be higher than those of normal rats.

For point-of-care testing, a miniaturized clot device was developed to measure the dynamic clot refraction forces using a small volume of whole blood.[140] In addition, a microfluidic dielectric sensor was introduced to measure multiple coagulation factors and platelet activity.[141]

3.3 Discussion on a haemorheological study under *ex vivo* conditions

Most previously developed techniques[43,44] still present technical limitations in continuous measurements of biophysical properties of blood. Firstly, after collecting blood samples from the closed loop repeatedly, blood viscosity or RBC aggregation was measured under *in vitro* conditions. Given that blood volume circulating in the closed loop decreased gradually, the total monitoring time was relatively short (less than 100–120 min). In addition, haemorheological properties, including viscosity and RBC aggregation, were repeatedly monitored at specific intervals of time instead of a continuous mode. To resolve these problems, haemorheological properties in closed-loop circulation must be measured without the collection of blood from the closed loop. Secondly, conventional methods utilise bulk-sized instruments, such as a microscope equipped with a high-speed camera for measuring fluid velocity or an ultrasonic imaging system for measuring RBC aggregation. Thus, they can be used only in laboratory environments equipped with expensive instruments. Evidently, detecting haemorheological properties with simple analytical sensors, including pressure sensors, flow rate sensors, vibrational spectroscopes and impedance analysers, is required. Lastly, previous methods focused on two haemorheological properties, namely, blood viscosity and RBC aggregation. Although RBC deformability or haematocrit is considered an effective parameter for detecting cardiovascular diseases,

previous methods did not provide information on RBC deformability under *ex vivo* conditions. Thus, multiple haemorheological properties, including blood viscosity, RBC aggregation and RBC deformability, need to be measured under *ex vivo* conditions.

4. Conclusions and perspectives

Biophysical properties of blood, including blood viscosity, RBC aggregation and RBC deformability, have been independently measured to monitor their variations in blood specimens collected from patients with haematological disorders. In this review, several techniques for measuring haemorheological properties (blood viscosity, RBC deformability and RBC aggregation) based on microfluidic platforms (*i.e. in vitro* condition) and extracorporeal bypass loops of animal models (*i.e. ex vivo* condition) were discussed. New technologies that can effectively and consistently provide comprehensive information on biophysical properties of blood circulating in the *ex vivo* closed loop are still needed. Firstly, commercialized products for the clinical measurement of haemorheological properties were summarized in Fig. S1 (ESI†). Most techniques were focused on a single property rather than multiple properties. An effective haemorheological index combined with several biophysical properties has not been proposed to diagnose haematological diseases under *in vitro* conditions. Thus, a blood-on-a-chip scheme needs to be developed for simultaneous measurements of haemorheological properties from a blood sample with a small volume. Secondly, most previous techniques are feasible under *in vitro* experimental conditions only. They require bulk-sized instruments, including a microscope for visualising blood flows and a high-speed camera for observing flow images. In addition, when an *in vitro* method is employed to measure haemorheological properties under *ex vivo* conditions, initial hemodilution is basically required to collect blood, and blood viscosity is then measured under *in vitro* conditions. However, hemodilution can alter the biophysical properties of blood measured for a short-term period of 100–130 min. To resolve these problems, a new analytical method should be developed for long-term and continuous measurements of haemorheological properties without hemodilution and periodic blood collection. Lastly, long polyethylene tubes are usually employed to connect a microfluidic device with blood vessels for establishing the extracorporeal rat bypass loop. Given that blood cells are in direct contact with a non-physiological surface, they adhere on the inner surface of the tube, which interrupts blood flows in a short-term period. To resolve this problem, the non-physiological surface must be reduced or removed by using elastomeric blood vessels[134,135] or implanted microfluidic devices.[136,137] In the near future, a new analytical methodology based on a microfluidic platform will be employed to diagnose haematological disorders and to screen effective treatment methods for curing them.

Conflicts of interest

There are no conflicts of interest to declare.

Acknowledgements

This work was supported by a National Research Foundation of Korea grant funded by the Korean Government (MSIP) (no. 2008-0061991). In addition, this work was supported by the Basic Science Research Program through NRF funded by the Ministry of Science, ICT and Future Planning (NRF-2018R1A1A1A05020389).

References

1 E. J. Benjamin, M. J. Blaha, S. E. Chiuve, M. Cushman, S. R. Das, R. Deo, S. D. d. Ferranti, J. Floyd, M. Fornage, C. Gillespie, *et al.*, *Circulation*, 2017, **135**, e146–e603.
2 P. C. Sousa, F. T. Pinho, M. A. Alves and M. S. N. Oliveira, *Korea-Aust. Rheol. J.*, 2016, **28**, 1–22.
3 J. Danesh, R. Collins, R. Peto and G. D. O. Lowe, *Eur. Heart J.*, 2000, **21**, 515–520.
4 J. Yayan, *Vasc. Health Risk Manage.*, 2012, **8**, 219–223.
5 A. L. Copley and G. V. F. Seaman, *Clin. Hemorheol.*, 1981, **1**, 117–119.
6 G. A. Pop, Z.-y. Chang, C. J. Slager, B.-J. Kooij, E. D. v. Deel, L. Moraru, J. Quak, G. C. Meijer and D. J. Duncker, *Biosens. Bioelectron.*, 2004, **19**, 1685–1693.
7 H. Y. Lee, C. Barber, J. A. Rogers and A. R. Minerick, *Electrophoresis*, 2015, **36**, 978–985.
8 S. Kim, R. L. Kong, A. S. Popel, M. Intaglietta and P. C. Johnson, *Am. J. Physiol.: Heart Circ. Physiol.*, 2007, **293**, H1526–H1535.
9 D. A. Fedosov, B. Caswell, A. S. Popel and G. E. Karniadakis, *Microcirculation*, 2010, **17**, 615–628.
10 R. Fahraeus and T. Lindqvist, *Am. J. Physiol.*, 1931, **96**, 562–568.
11 J. H. Barbee and G. R. Cokelet, *Microvasc. Res.*, 1971, **3**, 6–16.
12 T. M. Fischer, M. Sthohr-Liesen and H. Schmid-Schonbein, *Science*, 1978, **202**, 894–896.
13 G. Késmárky, P. Kenyeres, M. Rábai and K. Tóth, *Clin. Hemorheol. Microcirc.*, 2008, **39**, 243–246.
14 Y. J. Kang and S. Yang, *Microfluid. Nanofluid.*, 2013, **14**, 657–668.
15 Y. J. Kang, J. Ryu and S.-J. Lee, *Biomicrofluidics*, 2013, **7**, 044106.
16 S. Gupta, W. S. Wang and S. A. Vanapalli, *Biomicrofluidics*, 2016, **10**, 043402.
17 B. J. Ballermann, A. Dardik, E. Eng and A. Liu, *Kidney Int.*, 1998, **54**, S-100–S-108.
18 C. Spencer and G. Lip, *J. Hum. Hypertens.*, 2000, **14**, 291–293.

19 R. L. Letcher, S. Chien, T. G. Pickering, D. Phil, J. E. Sealey and J. H. Laragh, *Am. J. Med.*, 1981, **70**, 1195–1202.
20 Y. I. Cho, M. P. Mooney and D. J. Cho, *J. Diabetes Sci. Technol.*, 2008, **2**, 1130–1138.
21 Z. Wen, J. Xie, Z. Guan, D. Sun, W. Yao, K. Chen, Z.-y. Yan and Q. Mu, *Clin. Hemorheol. Microcirc.*, 2000, **22**, 261–266.
22 S. H. Song, J. H. Kim, J. H. Lee, Y.-M. Yun, D.-H. Choi and H. Y. Kim, *BMC Neurol.*, 2017, **17**, 20.
23 G. Lowe, A. Rumley, J. Norrie, I. Ford, J. Shepherd, S. Cobbe, P. Macfarlane and C. Packard, *Thromb. Haemostasis*, 2000, **84**, 553–558.
24 I. Velcheva, N. Antonova, E. Titianova, P. Damianov, N. Dimitrov and I. Ivanov, *Clin. Hemorheol. Microcirc.*, 2006, **35**, 195–198.
25 M. J. Santos, L. M. Pedro, H. Canhão, J. F. e. Fernandes, J. CanasdaSilva, J. E. Fonseca and C. Saldanha, *Atherosclerosis*, 2011, **219**, 821–826.
26 J. Ditzel, H. O. Bang and N. Thorsen, *J. Intern. Med.*, 1968, **183**, 577–579.
27 A. Groisman, M. Enzelberger and S. R. Quake, *Science*, 2003, **300**, 955–958.
28 M. Abkarian, M. Faivre and H. A. Stone, *Proc. Natl. Acad. Sci. U. S. A.*, 2006, **103**, 538–542.
29 S. A. Vanapalli, D. v. d. Ende, M. H. G. Duits and F. Mugele, *Appl. Phys. Lett.*, 2007, **90**, 114109.
30 S. A. Vanapalli, A. G. Banpurkar, D. v. d. Ende, M. H. G. Duits and F. Mugele, *Lab Chip*, 2009, **9**, 982–990.
31 P. Guillot, T. Moulin, R. Kötitz, M. Guirardel, A. Dodge, M. Joanicot, A. Colin, C.-H. Bruneau and T. Colin, *Microfluid. Nanofluid.*, 2008, **5**, 619–630.
32 D. E. Solomon and S. A. Vanapalli, *Microfluid. Nanofluid.*, 2014, **16**, 677–690.
33 P. Guillot and A. Colin, *Microfluid. Nanofluid.*, 2014, **17**, 605–611.
34 Y. J. Kang, *Analyst*, 2016, **141**, 6583–6597.
35 N.-T. Nguyen, Y.-F. Yap and A. Sumargo, *Meas. Sci. Technol.*, 2008, **19**, 085405.
36 B. K. Wunderlich and A. R. Bausch, *RSC Adv.*, 2013, **3**, 21730–21735.
37 S. Choi and J.-K. Park, *Small*, 2010, **6**, 1306–1310.
38 Y. J. Kang, S. Y. Yoon, K.-H. Lee and S. Yang, *Artif. Organs*, 2010, **34**, 944–949.
39 B. J. Kim, S. Y. Lee, S. Jee, A. Atajanov and S. Yang, *Sensors*, 2017, **17**, 1442.
40 E. Yeom, Y. J. Kang and S.-J. Lee, *Biomicrofluidics*, 2014, **8**, 034110.
41 Y. J. Kang and S.-J. Lee, *Biomicrofluidics*, 2013, **7**, 054122.
42 Y. J. Kang, E. Yeom and S.-J. Lee, *Biomicrofluidics*, 2013, **7**, 054111.
43 Y. J. Kang, E. Yeom and S.-J. Lee, *Anal. Chem.*, 2013, **85**, 10503–10511.
44 E. Yeom, Y. J. Kang and S.-J. Lee, *Sci. Rep.*, 2015, **5**, 11064.
45 K. Kang, L. J. Lee and K. W. Koelling, *Exp. Fluids*, 2005, **38**, 222–232.
46 S. D. Hudson, P. Sarangapani, J. A. Pathak and K. B. Migler, *J. Pharm. Sci.*, 2015, **104**, 678–685.
47 C. J. Pipe, T. S. Majmudar and G. H. McKinley, *Rheol. Acta*, 2008, **47**, 621–642.
48 J. Chevalier and F. Ayela, *Rev. Sci. Instrum.*, 2008, **79**, 076102.
49 T. Jung and S. Yang, *Sensors*, 2015, **15**, 11823–11835.
50 N. Srivastava, R. D. Davenport and M. A. Burns, *Anal. Chem.*, 2005, **77**, 383–392.
51 N. Srivastava and M. A. Burns, *Anal. Chem.*, 2006, **78**, 1690–1696.
52 N. Srivastava and M. A. Burns, *Lab Chip*, 2006, **6**, 744–751.
53 Z. Han, X. Tang and B. Zheng, *J. Micromech. Microeng.*, 2007, **17**, 1828–1834.
54 Z. Han and B. Zheng, *J. Micromech. Microeng.*, 2009, **19**, 115005.
55 D. E. Solomon, A. Abdel-Raziq and S. A. Vanapalli, *Rheol. Acta*, 2016, **55**, 727–738.
56 S. Oh, B. Kim, J. K. Lee and S. Choi, *Sens. Actuators, B*, 2018, **259**, 106–113.
57 H. Zeng and Y. Zhao, *Sens. Actuators, A*, 2011, **166**, 207–213.
58 M. Kim, A. Kim, S. Kim and S. Yang, *Biosens. Bioelectron.*, 2012, **35**, 416–420.
59 Y. J. Kang, E. Yeom, E. Seo and S.-J. Lee, *Biomicrofluidics*, 2014, **8**, 014102.
60 Y. J. Kang and S. Yang, *Lab Chip*, 2012, **12**, 1881–1889.
61 Y. J. Kang, *Sensors*, 2017, **17**, 2037.
62 Y. J. Kang, *Biomicrofluidics*, 2017, **11**, 014102.
63 X. Mao and T. J. Huang, *Lab Chip*, 2012, **12**, 4006–4009.
64 D. D. Carlo, *JALA*, 2012, **17**, 32–42.
65 Y. J. Kang, Y.-R. Ha and S.-J. Lee, *Anal. Chem.*, 2016, **88**, 2912–2922.
66 J. P. Shelby, J. White, K. Ganesan, P. K. Rathod and D. T. Chiu, *Proc. Natl. Acad. Sci. U. S. A.*, 2003, **100**, 14618–14622.
67 Y.-C. Chen, Y.-C. Lin, G.-Y. Chen and G.-J. Wang, *Microfluid. Nanofluid.*, 2010, **9**, 585–591.
68 T. Herricks, M. Antia and P. K. Rathod, *Cell. Microbiol.*, 2009, **11**, 1340–1353.
69 P. Preira, V. Grandne, J.-M. Forel, S. Gabriele, M. Camara and O. Theodoly, *Lab Chip*, 2013, **13**, 161–170.
70 Y. N. Luo, D. Y. Chen, Y. Zhao, C. Wei, X. T. Zhao, W. T. Yue, R. Long, J. B. Wang and J. Chen, *Sens. Actuators, B*, 2014, **202**, 1183–1189.
71 Q. Guo, S. J. Reiling, P. Rohrbach and H. Ma, *Lab Chip*, 2012, **12**, 1143–1150.
72 G. Mahmud, C. J. Campbell, K. J. M. Bishop, Y. A. Komarova, O. Chaga, S. Soh, S. Huda, K. Kandere-Grzybowska and B. A. Grzybowski, *Nat. Phys.*, 2009, **5**, 606–612.
73 R. O. Rodrigues, D. Pinho, V. Faustino and R. Lima, *Biomed. Microdevices*, 2015, **17**, 108.
74 H. W. Hou, A. A. S. Bhagat, A. G. L. Chong, P. Mao, K. S. W. Tan, J. Han and C. T. Lim, *Lab Chip*, 2010, **10**, 2605–2613.
75 M. J. Rosenbluth, W. A. Lam and D. A. Fletcher, *Lab Chip*, 2008, **8**, 1062–1070.

76 J. R. Lange, J. Steinwachs, T. Kolb, L. A. Lautscham, I. Harder, G. Whyte and B. Fabry, *Biophys. J.*, 2015, **109**, 26–34.
77 J. R. Lange, C. Metzner, S. Richter, W. Schneider, M. Spermann, T. Kolb, G. Whyte and B. Fabry, *Biophys. J.*, 2017, **112**, 1472–1480.
78 H. Bow, I. V. Pivkin, M. Diez-Silva, S. J. Goldfless, M. Dao, J. C. Niles, S. Suresh and J. Han, *Lab Chip*, 2011, **11**, 1065–1073.
79 S. S. Shevkoplyas, T. Yoshida, S. C. Gifford and M. W. Bitensky, *Lab Chip*, 2006, **6**, 914–920.
80 S. Youn, D. Lee and Y.-H. Cho, *J. Microelectromech. Syst.*, 2008, **17**, 302–308.
81 Q. Guo, S. P. Duffy, K. Matthews, X. Deng, A. T. Santoso, E. Islamzada and H. Ma, *Lab Chip*, 2016, **16**, 645–654.
82 E. S. Park, C. Jin, Q. Guo, R. R. Ang, S. P. Duffy, K. Matthews, A. Azad, H. Abdi, T. Todenhöfer, J. Bazov, *et al.*, *Small*, 2016, **12**, 1909–1919.
83 Y. J. Kang, Y.-R. Ha and S.-J. Lee, *Analyst*, 2016, **141**, 319–330.
84 J. M. A. Mauritz, T. Tiffert, R. Seear, F. Lautenschläger, A. Esposito, V. L. Lew, J. Guck and C. F. Kaminski, *J. Biomed. Opt.*, 2010, **15**, 030517.
85 E. Du, S. Ha, M. Diez-Silva, M. Dao, S. Suresh and A. P. Chandrakasan, *Lab Chip*, 2013, **13**, 3903–3909.
86 Y. Zheng, E. Shojaei-Baghini, A. Azad, C. Wang and Y. Sun, *Lab Chip*, 2012, **12**, 2560–2567.
87 Y. Zheng, J. Nguyen, Y. Wei and Y. Sun, *Lab Chip*, 2013, **13**, 2464–2483.
88 Z. Isiksacan, O. Erel and C. Elbuken, *Lab Chip*, 2016, **16**, 4682–4690.
89 K. Lee, C. Wagner and A. V. Priezzhev, *J. Biomed. Opt.*, 2017, **22**, 091516.
90 B. Neu and H. J. Meiselman, *Biophys. J.*, 2002, **83**, 2482–2490.
91 P. Steffen, C. Verdier and C. Wagner, *Phys. Rev. Lett.*, 2013, **110**, 018102.
92 Y. J. Kang, Y.-R. Ha and S.-J. Lee, *Biomicrofluidics*, 2014, **8**, 044114.
93 J.-X. Hou and S. Shin, *Korea-Aust. Rheol. J.*, 2008, **20**, 253–260.
94 H.-J. Lim, Y.-J. Lee, J.-H. Nam, S. Chung and S. Shin, *J. Biomech.*, 2010, **43**, 546–550.
95 J.-H. Nam, Y. Yang, S. Chung and S. Shin, *J. Biomed. Opt.*, 2010, **15**, 027003.
96 S. Shin, Y. Yang and J.-S. Suh, *Clin. Hemorheol. Microcirc.*, 2009, **41**, 197–207.
97 S. Shin, J. H. Jang, M. S. Park, Y. H. Ku and J. S. Suh, *Korea-Aust. Rheol. J.*, 2005, **17**, 9–13.
98 O. K. Baskurt, M. Uyuklu and H. J. Meiselman, *IEEE Trans. Biomed. Eng.*, 2010, **57**, 969–976.
99 N. Antonova, P. Riha and I. Ivanov, *Clin. Hemorheol. Microcirc.*, 2008, **39**, 69–78.
100 C. Balan, C. Balut, L. Gheorghe, C. Gheorghe, E. Gheorghiu and G. Ursu, *Clin. Hemorheol. Microcirc.*, 2004, **30**, 359–364.
101 A. Zhbanov and S. Yang, *PLoS One*, 2015, **10**, e0129337.
102 E. Kaliviotis, J. M. Sherwood and S. Balabani, *Sci. Rep.*, 2017, **7**, 44563.
103 J. M. Sherwood, J. Dusting, E. Kaliviotis and S. Balabani, *Biomicrofluidics*, 2012, **6**, 024119.
104 E. Yeom and S.-J. Lee, *Biomicrofluidics*, 2015, **9**, 024110.
105 M. Brust, O. Aouane, M. Thie'baud, D. Flormann, C. Verdier, L. Kaestner, M. W. Laschke, H. Selmi, A. Benyoussef, T. Podgorski, G. Coupier, C. Misbah and C. Wagner, *Sci. Rep.*, 2014, **4**, 4348.
106 G. Metry, M. Spittle, S. Rahmati, C. Giller, A. Giller, A. Kaufman, D. Schneditz, E. Manno, Z. Brener, I. Boniece, *et al.*, *Am. J. Kidney Dis.*, 2002, **40**, 996–1004.
107 Y. J. Kang, M. G. Kim, K. H. Son, C. H. Lim, H. S. Son, S. Y. Yoon, H. S. Kwon and S. Yang, *Artif. Organs*, 2010, **34**, E103–E109.
108 C. B. Ahn, Y. J. Kang, M. G. Kim, S. Yang, C. H. Lim, H. S. Son, J. S. Kim, S. Y. Lee, K. H. Son and K. Sun, *Korean J. Thorac. Cardiovasc. Surg.*, 2016, **49**, 145–150.
109 S. R. F. Whittaker and F. R. Winton, *J. Physiol.*, 1933, **78**, 339–369.
110 R. Fahraeus and R. Lindqvist, *Am. J. Physiol.*, 1931, **96**, 562–568.
111 S. Kim, R. L. Kong, A. S. Popel, M. Intaglietta and P. C. Johnson, *Am. J. Physiol.: Heart Circ. Physiol.*, 2007, **293**, H1526–H1535.
112 J. Zhang, P. C. Johnson and A. S. Popel, *Microvasc. Res.*, 2009, **77**, 265–272.
113 A. R. Pries and T. W. Secomb, *Am. J. Physiol.: Heart Circ. Physiol.*, 2005, **289**, H2657–H2664.
114 O. K. Baskurt, *Biorheology*, 2008, **45**, 629–638.
115 G. A. M. Pop, L. L. A. Bisschops, B. Iliev, P. C. Struijk, J. G. v. d. Hoeven and C. W. E. Hoedemaekers, *Biosens. Bioelectron.*, 2013, **41**, 595–601.
116 G. A. M. Pop, T. L. M. d. Backer, M. d. Jong, P. C. Struijk, L. Moraru, Z. Chang, H. G. Goovaerts, C. J. Slager and A. J. J. C. Bogers, *Eur. Surg. Res.*, 2004, **36**, 259–265.
117 E. I. Galanzha and V. P. Zharov, *Cytometry, Part A*, 2011, **79A**, 746–757.
118 J. Tripette, L.-C. Nguyen, L. Allard, P. Robillard, G. Soulez and G. Cloutier, *PLoS One*, 2015, **10**, e0124712.
119 W. Choi, H. M. Kim, S. Park, E. Yeom, J. Doh and S. J. Lee, *J. R. Soc., Interface*, 2017, **14**, 20160900.
120 J. J. Bishop, P. R. Nance, A. S. Popel, M. Intaglietta and P. C. Johnson, *Am. J. Physiol.: Heart Circ. Physiol.*, 2001, **280**, H222–H236.
121 A. Jaishankar, V. Sharma and G. H. McKinley, *Soft Matter*, 2011, **7**, 7623–7634.
122 A. Daly, J. S. Raval, J. H. Waters, M. H. Yazer and M. V. Kameneva, *Clin. Hemorheol. Microcirc.*, 2014, **56**, 337–345.
123 O. Yalcin, D. Ortiz, A. G. Tsai, P. C. Johnson and P. Cabrales, *Transfusion*, 2014, **54**, 1015–1027.
124 A. Hafezi-Moghadam, K. L. Thomas and C. Cornelssen, *Am. J. Physiol.: Cell Physiol.*, 2004, **286**, C876–C892.
125 A. Jain, A. Graveline, A. Waterhouse, A. Vernet, R. Flaumenhaft and D. E. Ingber, *Nat. Commun.*, 2016, **7**, 10176.

126 K.-H. Nam, E. Yeom and S.-J. Lee, *Microvasc. Res.*, 2012, **83**, 372–375.
127 E. Yeom, H. Byeon and S.-J. Lee, *Sci. Rep.*, 2016, **6**, 21913.
128 E. Yeom, H. M. Kim, J. H. Park, W. Choi, J. Doh and S.-J. Lee, *Sci. Rep.*, 2017, **7**, 1801.
129 K. Nagahashi, Y. Teramura and M. Takai, *Colloids Surf., B*, 2015, **134**, 384–391.
130 E. Yeom, J. H. Park, Y. J. Kang and S. J. Lee, *Sci. Rep.*, 2016, **6**, 24994.
131 M. Li, N. A. Hotaling, D. N. Ku and C. R. Forest, *PLoS One*, 2014, **9**, e82493.
132 J. Sibarani, M. Takai and K. Ishihara, *Colloids Surf., B*, 2007, **54**, 88–93.
133 T. V. Colace, G. W. Tormoen, O. J. T. McCarty and S. L. Diamond, *Annu. Rev. Biomed. Eng.*, 2013, **15**, 283–303.
134 W. Zhang, Y. S. Zhang, S. M. Bakht, J. Aleman, S. Shin, K. Yue, M. Sica, J. Ribas, M. Duchamp, J. Ju, *et al.*, *Lab Chip*, 2016, **16**, 1579–1586.
135 X.-Y. Wang, Y. Pei, M. Xie, Z.-H. Jin, Y.-S. Xiao, Y. Wang, L.-N. Zhang, Y. Lic and W.-H. Huang, *Lab Chip*, 2015, **15**, 1178–1187.
136 J. Kim, K. Yang, H.-J. Park, S. Han, Y. Shin, J. H. Lee, S. Chung and S.-W. Cho, *Biotechnol. Bioprocess Eng.*, 2014, **19**, 379–385.
137 H. Takehara, A. Nagaoka, J. Noguchi, T. Akagi, H. Kasai and T. Ichiki, *Sci. Rep.*, 2014, **4**, 6721.
138 H. Lee, G. Kim, C. Lim, B. Lee and S. Shin, *Biomicrofluidics*, 2016, **10**, 064118.
139 J. Zilberman-Rudenko, J. L. Sylman, H. H. S. Lakshmanan, O. J. T. McCarty and J. Maddala, *Cell. Mol. Bioeng.*, 2017, **10**, 16–29.
140 Z. Li, X. Li, B. McCracken, Y. Shao, K. Ward and J. Fu, *Small*, 2016, **12**, 3926–3934.
141 E. X. Stavrou, M. A. Suster, D. Maji, E. Kucukl, U. D. S. Sekhon, A. H. Schmaier, A. S. Gupta, U. A. Gurkan and P. Mohseni, *Blood*, 2016, **128**, 3754.